Summer 8-16-2018

Validation of Spatial Hysteresis as the Internal Damping Mechanism in an Unmanned Micro Aerial Vehicle Model

Ashleigh Chambers
Louisiana Tech University

VALIDATION OF SPATIAL HYSTERESIS AS THE INTERNAL DAMPING MECHANISM IN AN UNMANNED MICRO AERIAL VEHICLE MODEL

by

Ashleigh Chambers, B.S., M.S.

A Dissertation Presented in Partial Fulfillment
of the Requirements for the Degree
Doctor of Philosophy

COLLEGE OF ENGINEERING AND SCIENCE
LOUISIANA TECH UNIVERSITY

May 2018

Replace this page with the Signature Page.

Replace this page with the approval for scholarly dissemination form.

TABLE OF CONTENTS

LIST OF TABLES

LIST OF FIGURES

ACKNOWLEDGMENTS

To my advisor, Dr. Katie A. Evans: Thank you so much for your continued guidance, insight, and patience. I appreciate that you challenged me, while also encouraging me. You taught me so much and I cannot thank you enough.

To my committee: Thank you for your time and knowledge. I have learned so much from each of you, both during my project and in your classrooms.

To my undergraduate advisors, Drs. Stamatis Vokos and Amy Robertson: Thank you for believing in me. You pushed me to exceed and instilled an appreciation of education. For that, I am very grateful.

To my friends: Thank you for accepting my computer as an extension of myself. You never made me feel guilty when I brought work to hang out or when I was only half listening because I was also processing a problem. Your love and understanding has meant the world to me. Thanks for keeping me sane.

And, lastly, to my family: Thank you for your love and unconditional support. Mom, thanks for always encouraging me. You have always been there to offer an inspiring word. Dad, thanks for being my science fiction buddy. I owe a lot of my passion for science and love of knowledge to you. Nick, Maddie, Kaite, and Josh, I sacrificed a lot throughout my years in school, but the biggest was time with each of you. I appreciate your patience with me when I wasn't able to engage in your daily lives because I was busy. You all were my rock.

I feel so lucky to have had the support of so many amazing people. Without you all, this never would have been possible.

ABSTRACT

Unmanned aerial vehicles have been an area of interest in both research and industry for the past several decades. Advancements in technology have allowed such aircraft to decrease in size. UAVs are less expensive than traditional aircraft and are less restricted in where they can fly due to their compact size, leading to shifts in the way infrastructure, agriculture, and transportation surveillance and operations are handled.

However, small aerial vehicles and flexible, composite ones are more susceptible to crashes. This has led to an increased interest in methods to control such aircraft. In order to accurately model for a composite, flexible-wing aircraft, there is need for a more complex framework which takes into account the non-linear, spatially varying components associated with the frame. Throughout this project, the application under consideration is the internal damping coefficients.

In order to compare damping mechanisms, experiments were conducted in which a time history of the displacement at the tip of a cantilevered beam was measured. The optimal parameters were found for each model using a least squares cost equation for comparison with the measured data. These damping parameters were then incorporated into the generalized beam equation so that performance could be evaluated. This process was repeated for a variety of models.

This project builds upon previous studies on spatial hysteresis, a non-local internal form of damping. Spatial hysteresis damping was proposed as a damping model for large,

flexible, composite space structures. This method was first proposed by H.T. Banks and D.J. Inman for large space structures constructed of graphite epoxy composite materials (see, for example, [2], [9], [10]). These structures, due to their use in spacecraft, were much more rigid than the materials in which we are primarily interested.

Spatial hysteresis was not adopted on a large scale because it is computationally expensive. In the 1980s, when the model was proposed, it was extremely time consuming to incorporate spatial hysteresis using the current technology. Spatial hysteresis involves a kernel function and additional integration variable [8], [11], [15]. However, as computer processing power has increased, so has the potential to incorporate spatial hysteresis into the partial differential equation for a cantilevered beam. Due to this, recent research has proposed that such a damping model could also be used for composite, flexible wing UAVs ([16], [18], [19], [3]). These projects found that, by incorporating spatial hysteresis damping into an Euler Bernoulli beam model for a micro aerial vehicle (MAV), the aircraft was controlled more effectively in flight than by using Kelvin Voigt damping alone.

This work expands the field in that it merges two research areas: the experimental work done on space structures and theoretical work on applying spatial hysteresis to UAV models. It allows a theoretical form of internal damping to be experimentally validated for use in mathematical models of MAVs. This is significant because, by having a more complete understanding of composite, flexible wing materials, UAV development is more able to address control issues accurately and efficiently. With the boom of the UAV industry, there is a clear need for a mathematical model which accurately describes the materials used. This project aims to address that need.

CHAPTER 1

INTRODUCTION

1.1 Motivation

As the unmanned aerial vehicle market expands, modeling for the flight dynamics of such systems becomes very important. UAVs have continued to shrink in size due to technological advances in materials, fabrication, and control systems [1]. As such, their usefulness ranges from government operations to recreational use [7]. Companies, such as Amazon, are using UAVs to deliver packages to consumers [12]. Farmers track soil and crop health with the aid of drones [6]. Gas companies employ UAVs to examine pipelines. Cell phone companies, such as AT&T are using UAVs to inspect cell towers and their structural integrity [12]. Drones are being used to provide portable cell towers to increase cell signal during disasters or large events. Walmart is using UAVs to check inventory on a daily basis [12]. The cost effectiveness and versatility of using drones to fulfill common tasks drives much of the development in the UAV industry.

Despite all the advantages of using MAVs, such aircraft experience aerodynamical difficulties from the turbulent air flow, slow flight speed, and light weight of most MAVs. As such, micro aerial vehicles are notoriously difficult to control. Throughout this dissertation, we examine the material properties of flexible-wing aircraft in order to address such concerns.

1.2 Current Need

Flexible-wing, composite airframes use wings with materials that vary along the length of the wing since the wing is non-uniform in structure. There are significant property changes within composite materials making it imperative to construct a more accurate time and spatially varying partial differential model for such aircraft. Composites are more susceptible to property changes as they age [7]. This creates a clear need for a more active control system that assumes a material which has both a spatially and time varying component. Previous studies have examined a form of internal damping, called spatial hysteresis damping, for large, composite spacecraft [2]. Other projects have proposed that this model can be used in small, flexible, composite frames [3]. This project bridges the gap between the two by providing experimental validation for spatial hysteresis damping within a micro aerial vehicle model. Throughout this paper, viscous, Kelvin Voigt, and spatial hysteresis damping models will be considered.

1.3 Dissertation Outline

The dissertation outline is as follows. Chapter 2 provides an overview of past and current research into micro and biologically inspired UAVs. Chapter 3 provides necessary background information from basic beam theory, the Euler Bernoulli beam model, and damping models used throughout the remainder of the dissertation. Chapter 4 gives a numerical analysis for the mathematical basis of the project. It covers the traditional beam model, as well as spatially varying models, and provides the boundary conditions and numerical results for each one. Chapter 5 discusses the cantilever beam construction and vibrational analysis setup. Chapter 6 covers all experimental results for a single-layered,

double-layered, and triple-layered cantilever beam, as well as the error for each. Chapter 7 presents a comment on our findings, as well as other concluding remarks.

1.4 Contributions

This project adds several key findings to the field of micro aerial vehicles. It provides a numerical analysis for a beam model with spatially varying beam parameters, experimental validation of spatial hysteresis damping as applied to micro aerial vehicles, and a comparison of the damping parameters for beams of varying thickness and materials. This project has a strong backbone in previous research. It is based upon well-established work on the internal damping within large space structures [10]. This was expanded on by work that theorizes that spatial hysteresis would be a valuable model to use for flexible, composite unmanned aerial vehicle models [3]. These contributions are valuable because they allow for a more accurate understanding of the spatially-varying beam parameters within a composite, flexible-wing aircraft. This work bridges that gap by experimentally validating spatial hysteresis within a micro aerial vehicle. This is imperative information for the incorporation of controllers onto flexible, morphing wing surfaces.

CHAPTER 2

CURRENT RESEARCH

Unmanned aerial vehicles (UAVs) have been heavily researched from both a developmental and research perspective in the past several decades. Their usefulness ranges from military assessment operations, dangerous environment evaluation, and traffic surveillance to even more recreational usage like photography. Much of this development is driven by the practicality of flying UAVs where larger, manned aircraft cannot go due to navigation, size, speed, and cost constraints [5]. Despite these advantages, small UAVs are much more difficult to control due to the non-linear dynamics caused by low Reynolds numbers, flight speed on the order of wind gusts, and complex heave dynamics [7]. These limitations make it imperative to better understand the flight dynamics of a UAV in flight. Insight into the flight dynamics of such aircraft allow for better flight control, increased efficiency, and fewer crashes. As such, several different research groups have looked into new control measures [3].

2.1 Developmental

Flexible, morphing wings help reduce unpredictability in the flight dynamics of aircraft by adapting the lift-to-drag ratio when conditions change during a flight. This is a phenomenon realized with the first glider, the Wright Flyer, which was constructed by

Orville and Wilbur Wright. In the Wright Flyer, the pilot steered the plane by laying in the saddle and swaying his hips to twist the fabric and wood wings in response to air turbulence. However, as aircraft got heavier, wing adaptation was a practice which was discarded as it became impractical due to weight and control constraints [1].

There has been a renewed interest in morphing wings over the past few decades. Morphing wings improve aircraft performance, increase cost effectiveness, reduce drag, and reduce vibration. As such, there are several different companies interested in the integration of morphing wings onto aerial vehicles. Morphing wings rely on materials and actuators which modify wing geometry in different flight conditions. Industry has driven much of the morphing wing research, since the overall cost of fuel decreases as efficiency increases. Lockheed Martin has proposed a large aircraft platform with folding wings, Raytheon built wings that can extend in length during flight, and DARPA examined wings which are able to freely twist mid-flight [13]. Likewise, NASA and the Air Force created a FlexFoil, which increases fuel efficiency and reduces turbulence. During cruising, the FlexFoil flattens the wings trailing edge curvature. In turbulence, the trailing edge of the wing twists to redistribute the load as necessary. These wings are currently used on the Gulfstream III and are the first practical, lightweight, and durable shape-changing surfaces used on modern aircraft [12]. Lockheed Martin is also currently experimenting on a new airframe, the X-56A, which, although still not publically confirmed, is conjectured to have highly flexible, morphing wings [13].

In addition to creating surfaces which adapt during flight, several projects have examined using materials which can undergo property changes during flight. One area of interest has been shape memory alloys for flexible-wing micro aerial vehicles. These alloys

are able to undergo a phase transformation when under stress which allows them to recover from large strains [21]. These metals have a unique structure giving them the ability to morph into a new shape during a drastic temperature change. These materials have recently been incorporated into several morphing wing aerospace structures. These platforms have seen a decrease in vibration during flight and increased wing resiliency. Significant projects include a project with MIT and NASA which uses eight elements to construct a flexible wing. These wings are made of carbon fiber blocks each of a varying stiffness. The wing doesn't have ailerons or flaps, but instead twists in flight. Although they are not releasing details on the material, this study claims that the ability to twist is driven by materials which morph during differing flight conditions [21].

2.2 Research Interests

In the field of flexible, morphing wings, the flight dynamics of creatures such as bats, birds, and insects have revealed great insight into non-linear flight dynamics. Insect wings are inherently flexible, bat wings actively stretch, and birds morph their wing shape through moving both their joints and feathers [20]. The largest research collaboration studying such dynamics was funded by MURI. It involves researchers from Brown University, MIT, the University of Massachusetts, the University of Maryland, and Oregon State University. This study is interested in the flight mechanics and development of a UAV based on bat flight dynamics [6]. Bats are interesting from a research standpoint because they alter their wing structure, adjust their flapping motion, and can billow their wing membrane to achieve efficient flight. Bat wings are highly complex. Their motion is effected by several factors including flexibility, the structure of each bone, and the strength of the tendons and muscles

within the wing membrane. This group was able to study these motions and create the first fully developed 3D model for the kinematics of a bat in flight as seen in Figure 2.1 [6].

Figure 2.1: Bat in Flight from Reference 6

Several studies have examined the membrane on bat wings. A major component of the MURI work involved studying the wing membrane. The wing membrane allows the wing to completely transform and billow in different flight conditions. This provides insight into the flight dynamics of morphing-wing unmanned aerial vehicles [6]. Billowing is, in many ways, a difficult effect to emulate. It requires a strong skeletal structure, a thin, flexible membrane, and passive controllers which react to different wind conditions. As such, several projects have attempted to address issues of control and the irregular flight dynamics of membrane wings.

Wing shape adaptation has guided some development in understanding the flight dynamics of such flyers. A study done by Stanford examined the optimal wing shape and materials to understand the stability within such wing membranes. He used passive shape adaptation in the form of a flexible membrane to stabilize the aircraft. This work examined wing designs inspired by butterfly wings. During this study, he built on work done on wing shape topology and did testing on different wing shapes. Most significantly, he found that applying tension to the membrane before fabrication and using batten-enforced wing designs improves flight performance for flexible, composite aircraft and provided wind tunnel testing results more similat to that of a biological flier [1].

Other research has addressed the structural integrity of composite, flexible-wing micro aerial vehicles. One such study, done by Albert Lin, examined the manufacturing process for co-curing silicone onto composite MAV wings [4]. This research was motivated by an interest in the optimal wing topology and structure of a membrane wing. He studied flexible wings with a skeletal-based frame and was specifically interested in biologically inspired MAVs. This study consisted of wind tunnel testing to examine the surface deformation of different wing materials during flight. The most significant results of this project were to identify silicone as an ideal wing membrane, develop a manufacturing process for composite MAV wings, and experimentally validate the efficiency of different wing designs in order to create a micro aerial vehicle which operated similarly to a biological fllier [4].

By understanding biological flight dynamics and wing surfaces, researchers have significantly progressed the field of morphing, flexible wing UAVs. This information has

been used to make UAVs more efficient and less prone to crashes. However, there is still much to learn about the best way to control these surfaces.

CHAPTER 3

BACKGROUND INFORMATION

3.1 Beam Theory

Beams are defined as a structure in which one dimension, the length, is considerably larger than the other two [3]. Throughout this project, we have assumed a cantilevered Euler Bernoulli beam where the beam represents a single wing on a unmanned aerial vehicle. This is a standard representation with the cantilevered beam representing a single wing and the wall representing the fuselage or body of the aircraft.

3.1.1 Euler Bernoulli Beam

To begin, the beam diagram for such a model is shown in Figure 3.1.

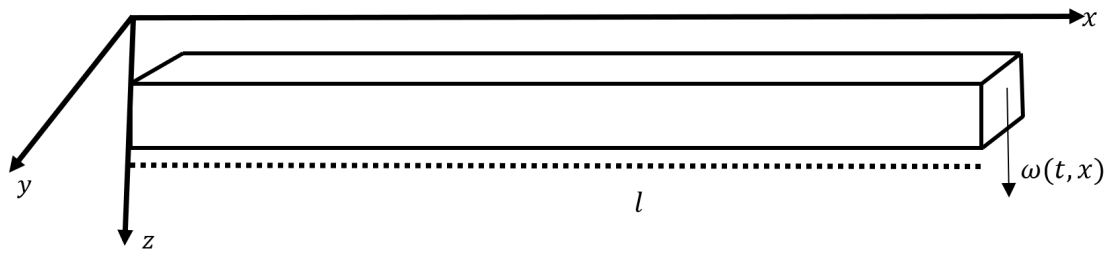

Figure 3.1: Euler Bernoulli Beam

where t is time, (x, y, z) is the position, $\omega(t, x)$ is the vertical displacement at time t and position x, and l is the length of the beam.

This model makes the following assumptions:

1. Symmetry: the longitudal axis is straight and the cross-section of the beam is perpendicular to it.
2. Normality: the plane sections normal to the longitudal axis remain plane and normal when the beam is deformed.
3. Strains: The internal strain in the beam is used to find the bending moment and deformation. Shear and axial force are assumed to be zero.
4. Linearization: We assume transverse rotation is small enough to be ignored.

The Euler Bernoulli model assumes that the internal energy loss within a beam is due to bending stress and strain. Using this model, we assume a beam resists transverse loads through bending action. This bending action produces compression on one side of the beam and tension in the other. The region between the two is called the neutral surface because it has zero stress [14]. The combination of these two types of stress cause a bending moment. If we consider a very small beam element subjected to a load, we can diagram the forces as seen in Figure 3.2.

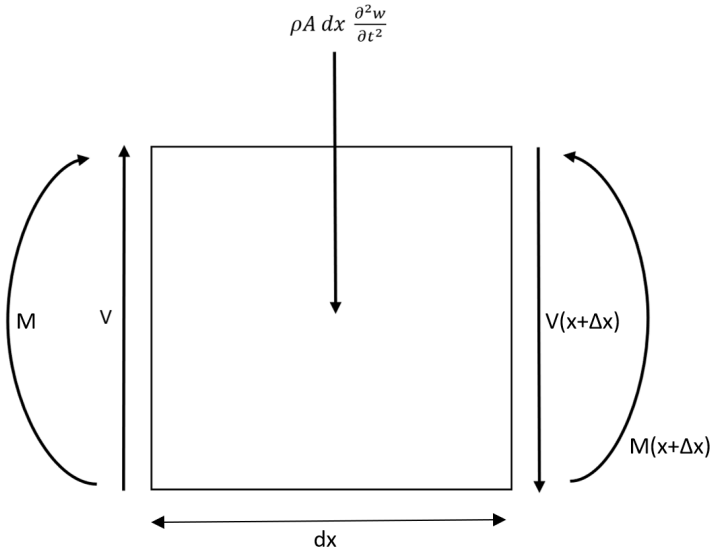

Figure 3.2: Moment and Shear Force of a Beam Element

where M is the bending moment, V is the shear force, x is the position at the left-hand side of the beam element, and $x+\Delta x$ is the position at the right-hand side of the beam element [7]. Since the vertical forces must be balanced, we have:

$$\rho A \frac{\partial^2}{\partial t^2} \omega(t,x) dx + V(x+\Delta x) - V(x) = 0 \tag{3.1}$$

We can approximate this:

$$\rho A \frac{\partial^2}{\partial t^2} \omega(t,x) dx = -V(\Delta x) \tag{3.2}$$

As is standard in beam theory, we can approximate:

$$M = EI \frac{\partial^2}{\partial x^2} \omega(t,x) \tag{3.3}$$

[14]. A cantilevered beam clamped at the position x=0 without a tip mass has the following boundary conditions:

$$\omega(t,0) = \omega_x(t,0) = 0 \tag{3.4}$$

since the fixed end requires both the displacement and slope to be zero at any time t.

Now, for the free end, we have the boundary conditions:

$$EI\omega_{xx}(t,l) = EI\omega_{xxx}(t,l) = 0 \tag{3.5}$$

since the free end requires that the sum of the moments and the sum of all forces on the free end be zero as long as only external damping is present.

Using the information above, the Euler Bernoulli cantilevered beam can be modeled using the following partial differential equation with generalized damping coefficients:

$$\omega_{tt}(t,x) + L_1\omega_t(t,x) + L_2\omega(t,x) + \frac{\partial^2}{\partial x^2}\left[\frac{EI}{\rho A}\omega_{xx}(t,x)\right] = f(t,x) \tag{3.6}$$

for $0 < x < l, t > 0$ where ρ is the mass density (mass per unit length) of the beam, A is the cross sectional area of the beam, EI is the flexural stiffness over the beam and is dependent on the location, $f(t,x)$ is the force input, and $\omega(t,x)$ is the beam displacement in the vertical direction. L_1 is the coefficient of the external damping mechanism and L_2 is the internal damping coefficient [2].

3.1.2 Flexible Wing Model

Now, assume we have a flexible-wing aircraft. Using this model, E varies throughout the length of the beam. The Euler Bernoulli beams becomes:

$$\omega_{tt}(t,x) + L_1\omega_t(t,x) + L_2\omega(t,x) + \frac{\partial^2}{\partial x^2}\left[\frac{E(x)I}{\rho A}\omega_{xx}(t,x)\right] = f(t,x) \tag{3.7}$$

where the variables are all defined as in the previous section. Likewise, the boundary conditions at the clamped end remain the same:

$$\omega(t,0) = \omega_x(t,0) = 0 \tag{3.8}$$

since the fixed end requires both the displacement and slope to be zero at any time t.

However, we will have to re-derive the equation for the moment and shear force. Since:

$$M = E(x)I\frac{\partial^2}{\partial x^2}\omega(t,x) \tag{3.9}$$

And:

$$-\frac{\partial^2 M}{\partial x^2} = E(x)I\frac{\partial^4}{\partial x^4}\omega(t,x) + 2E_x(x)I\frac{\partial^3}{\partial x^3}\omega(t,x) + E_{xx}(x)I\frac{\partial^2}{\partial x^2}\omega(t,x) \tag{3.10}$$

Now, for the free end, we have the boundary conditions:

$$E(l)I\omega_{xx}(t,l) = \frac{\partial}{\partial x}\left[E(l)I\omega_{xx}(t,l)\right] = 0 \tag{3.11}$$

since the free end requires that the sum of the moments and the sum of all forces on the free end be zero as long as only external damping is present. The case with internal damping coefficients will be addressed in Chapter 4.

3.1.3 Morphing Wing Model

Similarly, assume a morphing-wing micro aerial vehicle. We must account for the variability in the moment of inertia over the length of the wing. This would allow for a model in which we have a thin membrane over a carbon fiber skeleton. In this instance, the beam equation then is:

$$\omega_{tt}(t,x) + L_1\omega_t(t,x) + L_2\omega(t,x) + \frac{\partial^2}{\partial x^2}\left[\frac{EI(x)}{\rho A}\omega_{xx}(t,x)\right] = f(t,x) \tag{3.12}$$

where the variables are defined as in the previous section. Likewise, the boundary conditions remain the same at the clamped end as:

$$\omega(t,0) = \omega_x(t,0) = 0 \tag{3.13}$$

since the fixed end requires both the displacement and slope to be zero at any time t.

However, we will have to re-derive the equation for the moment and shear force. Since:

$$M = EI(x)\frac{\partial^2}{\partial x^2}\omega(t,x) \tag{3.14}$$

And:

$$-\frac{\partial^2 M}{\partial x^2} = EI(x)\frac{\partial^4}{\partial x^4}\omega(t,x) + 2EI_x(x)\frac{\partial^3}{\partial x^3}\omega(t,x) + EI_{xx}(x)\frac{\partial^2}{\partial x^2}\omega(t,x) \tag{3.15}$$

Now, for the free end, we have the boundary conditions:

$$EI(l)\omega_{xx}(t,l) = \frac{\partial}{\partial x}\left[EI(l)\omega_{xx}(t,l)\right] = 0 \tag{3.16}$$

since the free end requires that the sum of the moments and the sum of all forces on the free end be zero as long as only external damping is present. As before, the boundary conditions for a model with internal damping coefficients will be derived in the next chapter.

3.2 Damping Models

Damping is the dissipation of vibrational energy. As such, there are many different models on how to accurately describe damping in composite structures. Three main types of damping: viscous, Kelvin Voigt, and spatial hysteresis, as well as the combination of them will be compared in this analysis.

3.2.1 Viscous Air Damping

Typical damping models involve external viscous damping. In this case, the beam vibrates through the air, so the damping parameter is analagous to the air damping coefficient. This is the most straightforward method for modeling the damping of a beam. It assumes that a beam vibrating in air has a damping force proportional to the velocity of the beam

segment. This type of damping has the form:

$$L_1 = \gamma \tag{3.17}$$

where γ is the viscous damping constant of proportionality. For this form of damping, the beam equation with only viscous air damping is:

$$\rho A \omega_{tt}(t,x) + \gamma \omega_t(t,x) + EI\omega_{xxxx}(t,x) = f(t,x) \tag{3.18}$$

with boundary conditions:

$$\omega(t,0) = \omega_x(t,0) = 0 \tag{3.19}$$

$$EI\omega_{xx}(t,l) = 0 \tag{3.20}$$

$$EI\omega_{xxx}(t,l) = 0 \tag{3.21}$$

for the traditional, non-spatially varying, model. Both the flexible and the morphing wing boundary conditions will be covered more explicitly in Chapter 4.

3.2.2 Kelvin Voigt Damping

Commonly, Kelvin-Voigt damping, or strain rate damping, has been used to reflect the internal damping in structural models. It represents energy dissipated by internal friction in the beam and is of the form:

$$L_2 = c_d I \frac{\partial^5}{\partial x^4 \partial t} \tag{3.22}$$

where I is the moment of inertia and c_d is the strain rate damping coefficient. For this form of damping, the beam equation with only Kelvin Voigt damping is:

$$\rho A \omega_{tt}(t,x) + c_d I \omega_{xxxt}(t,x) + EI\omega_{xxxx}(t,x) = f(t,x) \tag{3.23}$$

with boundary conditions:

$$\omega(t,0) = \omega_x(t,0) = 0 \tag{3.24}$$

$$EI\omega_{xx}(t,l) + c_d I\omega_{xxt}(t,l) = 0 \tag{3.25}$$

$$EI\omega_{xxx}(t,l) + c_d I\omega_{xxxt}(t,x) = 0 \tag{3.26}$$

for the traditional model. Both the flexible and the morphing wing boundary conditions will be covered more explicitly in Chapter 4.

3.2.3 Spatial Hysteresis Damping

Another internal damping model that has been used for flexible structures is spatial hysteresis damping. This form of non-localized damping will be the main focus of my dissertation. Spatial hysteresis is based on interpreting the energy lost in the transverse vibration of a beam resulting from differential rates of rotation of neighboring beam sections causing internal friction. This is modeled by the equation:

$$\frac{\partial}{\partial x}\Big[\int_0^l h(x,\xi)[\omega_{xt}(t,x) - \omega_{xt}(t,\xi)]d\xi\Big] \tag{3.27}$$

where, the kernel is defined as:

$$h(x,\xi) = \frac{a}{b\sqrt{2\pi}} e^{-\frac{(x-\xi)^2}{2b^2}} \tag{3.28}$$

and a and b are constant damping coefficients [2]. For this form of damping, the beam equation with only spatial hysteresis damping is:

$$\rho A\omega_{tt}(t,x) + EI\omega_{xxxx}(t,x) - \frac{\partial}{\partial x}\Big[\int_0^l h(x,\xi)[\omega_{xt}(t,x) - \omega_{xt}(t,\xi)]d\xi\Big] = f(t,x) \tag{3.29}$$

With the boundary conditions:

$$\omega(t,0) = \omega_x(t,0) = 0 \tag{3.30}$$

$$EI\omega_{xx}(t,l) = 0 \tag{3.31}$$

$$EI\omega_{xxx}(t,l) - \Big[\int_0^l h(x,\xi)[\omega_{xt}(t,x) - \omega_{xt}(t,\xi)]d\xi\Big] = 0 \tag{3.32}$$

for the traditional, non-spatially varying, model. Both the flexible and the morphing wing boundary conditions will be covered more explicitly in Chapter 4.

CHAPTER 4

NUMERICAL ANALYSIS

4.1 Traditional Model

Since this dissertation is examining transverse vibrations of a cantilevered beam, we will use the generalized partial differential equation with the boundary conditions for internal and both external damping models assuming free vibration:

$$\omega_{tt}(t,x)+L_1\omega_t(t,x)+L_2\omega(t,x)+\frac{\partial^2}{\partial x^2}\Big[\frac{EI}{\rho A}\omega_{xx}(t,x)\Big]=0 \tag{4.1}$$

for $0 \leq x \leq l$ and $t \geq 0$. The boundary conditions are:

$$\omega(t,0)=\frac{\partial \omega}{\partial x}(t,0)=0, \tag{4.2}$$

$$EI\omega_{xx}(t,l)+c_dI\omega_{xxt}(t,l)=0, \tag{4.3}$$

$$\frac{\partial}{\partial x}[EI\omega_{xx}(t,l)+c_dI\omega_{xxt}(t,l)]-\Big[\int_0^l h(x,\xi)(\omega_{xt}(t,x)-\omega_{xt}(t,\xi))d\xi\Big]\Big|^l=0. \tag{4.4}$$

Any simulation involving fewer forms of damping will use the boundary conditions outlined in Chapter 3.

Assuming all forms of damping, the beam model becomes:

$$\rho A\omega_{tt}(t,x)+\gamma\omega_t(t,x)+c_dI\omega_{txxxx}(t,x)+EI\omega_{xxxx}(t,x)- \frac{\partial}{\partial x}\Big[\int_0^l h(x,\xi)[\omega_{xt}(t,x)-\omega_{xt}(t,\xi)]d\xi\Big]=0. \tag{4.5}$$

4.1.1 Weak Formulation

We use the Galerkin Finite Element method to find numerical solutions to the Euler Bernoulli beam model. As is standard in finite elements, we multiply the beam equation by the test function $\phi(x) \in H^2(0,l)$ to obtain:

$$\rho A\omega_{tt}(t,x)\phi(x) + \gamma\omega_t(t,x)\phi(x) + c_d I\omega_{txxxx}(t,x)\phi(x) + EI\omega_{xxxx}(t,x)\phi(x) - \frac{\partial}{\partial x}\Big[\int_0^l h(x,\xi)[\omega_{xt}(t,x) - \omega_{xt}(t,\xi)]d\xi\Big]\phi(x) = 0. \quad (4.6)$$

Now, integrate with respect to x:

$$\int_0^l \rho A\omega_{tt}(t,x)\phi(x)dx + \int_0^l \gamma\omega_t(t,x)\phi(x)dx + \int_0^l c_d I\omega_{txxxx}(t,x)\phi(x)dx + \int_0^l EI\omega_{xxxx}(t,x)\phi(x)dx - \int_0^l \frac{\partial}{\partial x}\Big[\int_0^l h(x,\xi)[\omega_{xt}(t,x) - \omega_{xt}(t,\xi)]d\xi\Big]\phi(x)dx = 0. \quad (4.7)$$

To make this a 2nd order partial differential equation, we need to integrate the 3rd term by parts:

$$\int_0^l c_d I\omega_{txxxx}(t,x)\phi(x)dx = c_d I\omega_{txxx}(t,x)\phi(x)|_0^l - \int_0^l c_d I\omega_{txxx}(t,x)\phi_x(x)dx. \quad (4.8)$$

So, applying integration by parts again:

$$\int_0^l c_d I\omega_{txxx}(t,x)\phi_x(x)dx = c_d I\omega_{txx}(t,x)\phi_x(x)|_0^l - \int_0^l c_d I\omega_{txx}(t,x)\phi_{xx}(x)dx, \quad (4.9)$$

And:

$$\int_0^l c_d I\omega_{txxxx}(t,x)\phi(x)dx = c_d I\omega_{txxx}(t,x)\phi(x)|_0^l - c_d I\omega_{txx}(t,x)\phi_x(x)|_0^l + \int_0^l c_d I\omega_{txx}(t,x)\phi_{xx}(x)dx. \quad (4.10)$$

Applying the boundary conditions to this term:

$$\int_0^l c_d I\omega_{txxxx}(t,x)\phi(x)dx = c_d I\omega_{txxx}(t,l)\phi(l) - c_d I\omega_{txx}(t,l)\phi_x(l) + \int_0^l c_d I\omega_{txx}(t,x)\phi_{xx}(x)dx. \quad (4.11)$$

Likewise, we integrate the 4th term by parts:

$$EI\omega_{xxxx}(t,x)\phi(x)dx = EI\omega_{xxx}(t,x)\phi(x)|_0^l - \int_0^l EI\omega_{xxx}(t,x)\phi_x(x)dx \quad (4.12)$$

And applying integration by parts again:

$$\int_0^l EI\omega_{xxx}(t,x)\phi_x(x)dx = EI\omega_{xx}(t,x)\phi_x(x)|_0^l - \int_0^l EI\omega_{xx}(t,x)\phi_{xx}(x)dx. \quad (4.13)$$

So:

$$EI\omega_{xxxx}(t,x)\phi(x)dx = EI\omega_{xxx}(t,x)\phi(x)|_0^l - EI\omega_{xx}(t,x)\phi_x(x)|_0^l + \int_0^l EI\omega_{xx}(t,x)\phi_{xx}(x)dx. \quad (4.14)$$

Now, applying the boundary conditions to this term:

$$EI\omega_{xxxx}(t,x)\phi(x)dx = EI\omega_{xxx}(t,l)\phi(l) - EI\omega_{xx}(t,l)\phi_x(l) + \int_0^l EI\omega_{xx}(t,x)\phi_{xx}(x)dx \quad (4.15)$$

In order to apply the boundary conditions, we are also going to integrate the spatial hysteresis term by parts:

$$\int_0^l \frac{\partial}{\partial x}\Big[\int_0^l h(x,\xi)[\omega_{xt}(t,x) - \omega_{xt}(t,\xi)]d\xi\Big]\phi(x)dx = \phi(x)\int_0^l h(x,\xi)[\omega_{xt}(t,x) - \omega_{xt}(t,\xi)]d\xi|_0^l - \int_0^l \Big[\int_0^l h(x,\xi)[\omega_{xt}(t,x) - \omega_{xt}(t,\xi)]d\xi\Big]\phi_x(x)dx \quad (4.16)$$

The weak form is now:

$$\int_0^l \rho A\omega_{tt}(t,x)\phi(x)dx+\int_0^l \gamma\omega_t(t,x)\phi(x)dx+c_dI\omega_{txxx}(t,l)\phi(l)-c_dI\omega_{txx}(t,l)\phi_x(l)+$$
$$\int_0^l c_dI\omega_{txx}(t,x)\phi_{xx}(x)dx+EI\omega_{xxx}(t,x)\phi(x)|_0^l-EI\omega_{xx}(t,x)\phi_x(x)|_0^l+$$
$$\int_0^l EI\omega_{xx}(t,x)\phi_{xx}(x)dx-\phi(x)\int_0^l h(x,\xi)[\omega_{xt}(t,x)-\omega_{xt}(t,\xi)]d\xi|_0^l+$$
$$\int_0^l \Big[\int_0^l h(x,\xi)[\omega_{xt}(t,x)-\omega_{xt}(t,\xi)]d\xi\Big]\phi_x(x)dx=0 \quad (4.17)$$

Apply the appropriate boundary conditions for the free end and we have:

$$\int_0^l \rho A\omega_{tt}(t,x)\phi(x)dx+\int_0^l \gamma\omega_t(t,x)\phi(x)dx+\int_0^l c_dI\omega_{txx}(t,x)\phi_{xx}(x)dx+$$
$$\int_0^l EI\omega_{xx}(t,x)\phi_{xx}(x)dx+\int_0^l \Big[\int_0^l h(x,\xi)[\omega_{xt}(t,x)-\omega_{xt}(t,\xi)]d\xi\Big]\phi_x(x)dx=0. \quad (4.18)$$

4.1.2 Cubic Hermitian Polynomials

Now that we have found the weak form of the equation, we are able to approximate the displacement of the beam using cubic Hermite polynomials. This method divides the beam into N subintervals:

$$\omega(t,x)\cong\omega^N(t,s)=\sum_{i=1}^N c_i(t)\phi_i(x), \quad (4.19)$$

where $\phi_i(x)$ are the spatially dependent cubic spline basis functions and $c_i(t)$ are the time dependent coefficients.

Substituting (4.19) into (4.18), we get the equation:

$$\int_0^l \rho A\sum_{i=1}^N \ddot{c}_i(t)\phi_i(x)\phi(x)dx+\int_0^l \gamma\sum_{i=1}^N \dot{c}_i(t)\phi_i(x)\phi(x)dx+$$
$$\int_0^l EI\sum_{i=1}^N c_i(t)\phi_i''(x)\phi''(x)dx+\int_0^l c_dI\sum_{i=1}^N \dot{c}_i(t)\phi_i''(x)\phi''(x)dx-$$
$$\int_0^l \Big[\int_0^l h(x,\xi)\sum_{i=1}^N[\dot{c}_i(t)\phi_i'(x)-\dot{c}_i(t)\phi_i'(\xi)\Big]d\xi\,\phi'(x)dx=0. \quad (4.20)$$

where $\dot{c} = c_t$ and $\phi' = \phi_x$.

Choosing a function $\phi(x)$ with a range over the basis function of $\phi_j(x)$ for $j = 1,2,...,N$ and simplifying:

$$\rho A \sum_{i=1}^{N} \ddot{c}_i(t) \int_0^l \phi_i(x)\phi_j(x)dx + \gamma \sum_{i=1}^{N} \dot{c}_i(t) \int_0^l \phi_i(x)\phi_j(x)dx + EI \sum_{i=1}^{N} c_i(t) \int_0^l \phi_i''(x)\phi_j''(x)dx + c_d I \sum_{i=1}^{N} \dot{c}_i(t) \int_0^l \phi_i''(x)\phi_j''(x)dx - \sum_{i=1}^{N} \dot{c}_i(t) \int_0^l \int_0^l h(x,\xi)[\phi_i'(x) - \phi_i'(\xi))]d\xi\, \phi_j'(x)dx = 0. \quad (4.21)$$

This can be rewritten:

$$\rho A \begin{bmatrix} \ddot{c}_1(t) \\ ... \\ \ddot{c}_N(t) \end{bmatrix} \begin{bmatrix} \int_0^l \phi_1(x)\phi_1(x) & ... & \int_0^l \phi_1(x)\phi_N(x) \\ ... & ... & ... \\ \int_0^l \phi_N(x)\phi_j(x) & ... & \int_0^l \phi_N(x)\phi_N(x) \end{bmatrix} + \gamma \begin{bmatrix} \dot{c}_1(t) \\ ... \\ \dot{c}_N(t) \end{bmatrix} \quad (4.22)$$

$$\begin{bmatrix} \int_0^l \phi_1(x)\phi_1(x) & ... & \int_0^l \phi_1(x)\phi_N(x) \\ ... & ... & ... \\ \int_0^l \phi_N(x)\phi_j(x) & ... & \int_0^l \phi_N(x)\phi_N(x) \end{bmatrix} + EI \begin{bmatrix} c_1(t) \\ ... \\ c_N(t) \end{bmatrix} \begin{bmatrix} \int_0^l \phi_1''(x)\phi_1''(x) & ... & \int_0^l \phi_1''(x)\phi_N''(x) \\ ... & ... & ... \\ \int_0^l \phi_N(x)\phi_j''(x) & ... & \int_0^l \phi_N(x)\phi_N''(x) \end{bmatrix} \quad (4.23)$$

$$+c_d I \begin{bmatrix} \dot{c}_1(t) \\ ... \\ \dot{c}_N(t) \end{bmatrix} \begin{bmatrix} \int_0^l \phi_1''(x)\phi_1''(x) & ... & \int_0^l \phi_1''(x)\phi_N''(x) \\ ... & ... & ... \\ \int_0^l \phi_N(x)\phi_j''(x) & ... & \int_0^l \phi_N(x)\phi_N''(x) \end{bmatrix} + \begin{bmatrix} \dot{c}_1(t) \\ ... \\ \dot{c}_N(t) \end{bmatrix} \quad (4.24)$$

$$\begin{bmatrix} \int_0^l \int_0^l h(x,\xi)[\phi_1'(x) - \phi_1'(\xi)]d\xi\, \phi_1'(x)dx & ... & \int_0^l \int_0^l h(x,\xi)[\phi_1'(x) - \phi_1'(\xi)]d\xi\, \phi_N'(x)dx \\ ... & ... & ... \\ \int_0^l \int_0^l h(x,\xi)[\phi_N'(x) - \phi_N'(\xi)]d\xi\, \phi_1'(x)dx & ... & \int_0^l \int_0^l h(x,\xi)[\phi_N'(x) - \phi_N'(\xi)]d\xi\, \phi_N'(x)dx \end{bmatrix} = 0 \quad (4.25)$$

Rewriting and grouping all like terms, we obtain the matrix system:

$$M\ddot{c}(t) + D\dot{c}(t) + Kc(t) = 0 \tag{4.26}$$

The system matrices are defined as:

$$[M]_{i,j} = \rho A \int_0^l \phi_i(x)\phi_j(x)dx \tag{4.27}$$

$$[K]_{i,j} = EI \int_0^l \phi_i''(x)\phi_j''(x)dx \tag{4.28}$$

$$[D]_{i,j} = \gamma \int_0^l \phi_i(x)\phi_j(x)dx + c_d I \int_0^l \phi_i''(x)\phi_j''(x)dx + \int_0^l \Big[\int_0^l h(x,\xi)[\phi_i'(x) - \phi_i'(\xi)]d\xi \Big] \phi_j'(x)dx \tag{4.29}$$

We can rewrite (4.26) as:

$$\ddot{c}(t) = M^{-1}(-D\dot{c}(t) - Kc(t)) \tag{4.30}$$

Finally, we let:

$$x_1(t) = c(t) \tag{4.31}$$

$$x_2(t) = \dot{x}_1(t) = \dot{c}(t) \tag{4.32}$$

Now,

$$\dot{x}_2(t) = M^{-1}(-Dx_2(t) - Kx_1(t)) \tag{4.33}$$

Which can be written as a first order system of ODEs as:

$$\dot{x}(t) = Ax(t) \tag{4.34}$$

where:

$$x(t) = \begin{bmatrix} c(t) \\ \dot{c}(t) \end{bmatrix} \tag{4.35}$$

and

$$A = \begin{bmatrix} 0 & I \\ -M^{-1}K & -M^{-1}D \end{bmatrix} \tag{4.36}$$

This is then a first order ordinary differential equation that can be solved through traditional numerical methods. In this case, the technique used was a six-step, fifth-order Runge-Kutta in Matlab.

Now that we have approximated a solution to the beam model, we are able to use inverse parameter estimation to compare all three damping models to experimental results. We use the measured time history of the lateral vibration at the tip of the beam. The problem then becomes a cost-minimization of the form:

$$J^N(q) = \sum_{i=1}^{M} |\omega^N(t,l,q) - \hat{\omega}(t,l)|^2 \tag{4.37}$$

where $\omega(t,x,q)$ denotes a solution with the appropriate boundary and initial conditions based on the parameter values and M is the number of tip displacement measurements. Using the Nelder-Mead simplex algorithm in Matlab, which takes an initial parameter estimate and converges on the optimal parameter value by moving towards a more accurate model, this cost equation converges to q^*, the vector of parameters which best fit the experimental data.

4.2 Flexible Wing Model

Since we are interested in the application of such a model to flexible-wing micro aerial vehicles, we want to examine the mathematical model used when the wing elasticity

varies over the length. As such, we are going to approximate the solution to a spatially varying cantilever beam using the same basic method as in the previous section. We will use the generalized partial differential equation with the boundary conditions for internal and both external damping models assuming free vibration:

$$\omega_{tt}(t,x)+L_1\omega_t(t,x)+L_2\omega(t,x)+\frac{\partial^2}{\partial x^2}\big[\frac{E(x)I}{\rho A}\omega_{xx}(t,x)\big]=0 \tag{4.38}$$

for $0\leq x\leq l$ and $t\geq 0$ where the boundary conditions are:

$$\omega(t,0)=\frac{\partial\omega}{\partial x}(t,0)=0, \tag{4.39}$$

$$E(l)I\omega_{xx}(t,l)+c_dI\omega_{xxt}(t,l)=0 \tag{4.40}$$

$$\frac{\partial}{\partial x}[E(l)I\omega_{xx}(t,l)+c_dI\omega_{xxt}(t,l)]-\Big[\int_0^l h(x,\xi)(\omega_{xt}(t,x)-\omega_{xt}(t,\xi))d\xi\Big]|^l=0 \tag{4.41}$$

where any simulation involving fewer forms of damping will use the boundary conditions outlined in Chapter 3.

Assuming all forms of damping, the beam model becomes:

$$\rho A\omega_{tt}(t,x)+\gamma\omega_t(t,x)+c_dI\omega_{txxxx}(t,x)+E(x)I\omega_{xxxx}(t,x)+$$
$$E_{xx}(x)I\omega_{xx}(t,x)+2E_x(x)I\omega_{xxx}(t,x)-$$
$$\frac{\partial}{\partial x}\Big[\int_0^l h(x,\xi)[\omega_{xt}(t,x)-\omega_{xt}(t,\xi)]d\xi\Big]=0 \tag{4.42}$$

4.2.1 Weak Formulation

We will approximate the solution to the beam equation using the Galerkin Finite Element method, as before. First, we multiply the beam equation by the test function $\phi(x)\in H^2(0,l)$ to obtain:

$$\rho A\omega_{tt}(t,x)\phi(x)+\gamma\omega_t(t,x)\phi(x)+c_dI\omega_{txxxx}(t,x)\phi(x)+E(x)I\omega_{xxxx}(t,x)\phi(x)+$$
$$E_{xx}(x)I\omega_{xx}(t,x)\phi(x)+2E_x(x)I\omega_{xxx}(t,x)\phi(x)-$$
$$\frac{\partial}{\partial x}\Big[\int_0^l h(x,\xi)[\omega_{xt}(t,x)-\omega_{xt}(t,\xi)]d\xi\Big]\phi(x)=0 \quad (4.43)$$

Integrate with respect to x:

$$\int_0^l \rho A\omega_{tt}(t,x)\phi(x)dx+\int_0^l \gamma\omega_t(t,x)\phi(x)dx+\int_0^l c_dI\omega_{txxxx}(t,x)\phi(x)dx+$$
$$\int_0^l E_{xx}(x)I\omega_{xx}(t,x)\phi(x)dx+2\int_0^l E_x(x)I\omega_{xxx}(t,x)\phi(x)dx+$$
$$\int_0^l E(x)I\omega_{xxxx}(t,x)\phi(x)dx-\int_0^l \frac{\partial}{\partial x}\Big[\int_0^l h(x,\xi)[\omega_{xt}(t,x)-\omega_{xt}(t,\xi)]d\xi\Big]\phi(x)dx=0. \quad (4.44)$$

Now, integrate the 3rd term by parts twice, as before, and apply the boundary conditions:

$$\int_0^l c_dI\omega_{txxxx}(t,x)\phi(x)dx=c_dI\omega_{txxx}(t,l)\phi(l)-c_dI\omega_{txx}(t,l)\phi_x(l)+$$
$$\int_0^l c_dI\omega_{txx}(t,x)\phi_{xx}(x)dx. \quad (4.45)$$

Likewise, we integrate the 6th term by parts:

$$\int_0^l E(x)I\omega_{xxxx}(t,x)\phi(x)dx=E(x)I\omega_{xxx}(t,x)\phi(x)|_0^l-\int_0^l E_x(x)I\omega_{xxx}(t,x)\phi(x)dx-$$
$$\int_0^l E(x)I\omega_{xxx}(t,x)\phi_x(x)dx \quad (4.46)$$

Integrating by parts again (first, to the second term and then to the third term):

$$\int_0^l E_x(x)I\omega_{xxx}(t,x)\phi(x)dx=E_x(x)I\omega_{xx}(t,x)\phi(x)|_0^l-\int_0^l E_{xx}(x)I\omega_{xx}(t,x)\phi(x)dx-$$
$$\int_0^l E_x(x)I\omega_{xx}(t,x)\phi_x(x)dx \quad (4.47)$$

And,

$$\int_0^l E(x)I\omega_{xxx}(t,x)\phi_x(x)dx = E(x)I\omega_{xx}(t,x)\phi_x(x)|_0^l - \int_0^l E_x(x)I\omega_{xx}(t,x)\phi_x(x)dx - \int_0^l E(x)I\omega_{xx}(t,x)\phi_{xx}(x)dx \quad (4.48)$$

So:

$$\int_0^l E(x)I\omega_{xxxx}(t,x)\phi(x)dx = E(x)I\omega_{xxx}(t,x)\phi(x)|_0^l - E_x(x)I\omega_{xx}(t,x)\phi(x)|_0^l + \int_0^l E_{xx}I\omega_{xx}(t,x)\phi(x)dx + \int_0^l E_x(x)I\omega_{xx}(t,x)\phi_x(x)dx - E(x)I\omega_{xx}(t,x)\phi_x(x)|_0^l + \int_0^l E_x(x)I\omega_{xx}(t,x)\phi_x(x)dx + \int_0^l E(x)I\omega_{xx}(t,x)\phi_{xx}(x)dx \quad (4.49)$$

Applying the boundary conditions to this term:

$$E(x)I\omega_{xxxx}(t,x)\phi(x)dx = E(l)I\omega_{xxx}(t,l)\phi(l) - E_x(l)I\omega_{xx}(t,l)\phi(l) - E(L)I\omega_{xx}(t,l)\phi_x(l) \int_0^l E_{xx}I(x)\omega_{xx}(t,x)\phi(x)dx + 2\int_0^l E_x(x)I\omega_{xx}(t,x)\phi_x(x)dx + \int_0^l E(x)I\omega_{xx}(t,x)\phi_{xx}(x)dx \quad (4.50)$$

Lastly,

$$2\int_0^l E_x(x)I\omega_{xxx}(t,x)\phi(x)dx = 2E_x(x)I\omega_{xx}(t,x)\phi(x)|_0^l - \int_0^l 2E_{xx}(x)I\omega_{xx}(t,x)\phi(x)dx - \int_0^l 2E_xI\omega_{xx}(t,x)\phi_x(x)dx \quad (4.51)$$

In order to apply the boundary conditions, we are also going to integrate the spatial hysteresis term by parts, as before. The weak form is now:

$$\int_0^l \rho A\omega_{tt}(t,x)\phi(x)dx + \int_0^l \gamma\omega_t(t,x)\phi(x)dx + c_dI\omega_{txxx}(t,l)\phi(l) - c_dI\omega_{txx}(t,l)\phi_x(l) + \int_0^l c_dI\omega_{txx}(t,x)\phi_{xx}(x)dx + E(l)I\omega_{xxx}(t,l)\phi(l) - E_x(l)I\omega_{xx}(t,l)\phi(l) - E(l)I\omega_{xx}(t,l)\phi_x(l) + \int_0^l E_{xx}I\omega_{xx}(t,x)\phi(x)dx +$$

$$2E_x(x)I\omega_{xx}(t,x)\phi(x)|_0^l - \int_0^l 2E_{xx}(x)I\omega_{xx}(t,x)\phi(x)dx -$$
$$\int_0^l 2E_xI\omega_{xx}(t,x)\phi_x(x)dx + \int_0^l E_{xx}(x)I\omega_{xx}(t,x)\phi(x)dx +$$
$$2\int_0^l E_x(x)I\omega_{xx}(t,x)\phi_x(x)dx + \int_0^l E(x)I\omega_{xx}(t,x)\phi_{xx}(x)dx -$$
$$\phi(x)\int_0^l h(x,\xi)[\omega_{xt}(t,x)-\omega_{xt}(t,\xi)]d\xi\,|_0^l + \int_0^l [\int_0^l h(x,\xi)[\omega_{xt}(t,x)-\omega_{xt}(t,\xi)]d\xi]\phi_x(x)dx = 0 \tag{4.52}$$

Apply the appropriate boundary conditions for the free end and we have:

$$\int_0^l \rho A\omega_{tt}(t,x)\phi(x)dx + \int_0^l \gamma\omega_t(t,x)\phi(x)dx + \int_0^l c_dI\omega_{txx}(t,x)\phi_{xx}(x)dx$$
$$+ \int_0^l E(x)I\omega_{xx}(t,x)\phi_{xx}(x)dx + \int_0^l \Big[\int_0^l h(x,\xi)[\omega_{xt}(t,x)-\omega_{xt}(t,\xi)]d\xi\Big]\phi_x(x)dx = 0 \tag{4.53}$$

4.2.2 Cubic Hermitian Polynomials

Now that we have found the weak form of the equation, we are able to approximate the displacement of the beam using cubic Hermite polynomials. This method divides the beam into N subintervals:

$$\omega(t,x) \cong \omega^N(t,s) = \sum_{i=1}^{N} c_i(t)\phi_i(x), \tag{4.54}$$

where $\phi_i(x)$ are the spatially dependent cubic spline basis functions and $c_i(t)$ are the time dependent coefficients.

Substituting this into the beam equation, we arrive at:

$$\int_0^l \rho A\sum_{i=1}^{N}\ddot{c}_i(t)\phi_i(x)\phi(x)dx + \int_0^l \gamma\sum_{i=1}^{N}\dot{c}_i(t)\phi_i(x)\phi(x)dx +$$
$$\int_0^l c_dI\sum_{i=1}^{N}\dot{c}_i(t)\phi_i''(x)\phi(x)dx + \int_0^l I\sum_{i=1}^{N}c_i(t)\phi_i''(x)E(x)\phi''(x)dx +$$

$$\int_0^l \Big[\int_0^l h(x,\xi) \sum_{i=1}^{N} [\dot{c}_i(t)\phi_i'(x) - \dot{c}_i(t)\phi_i'(\xi)] d\xi \Big] \phi'(x) dx = 0. \quad (4.55)$$

where $\dot{c} = c_t$ and $\phi' = \phi_x$.

Choosing a function $\phi(x)$ with a range over the basis function of $\phi_j(x)$ for $j = 1, 2, ..., N$ and simplifying:

$$\rho A \sum_{i=1}^{N} \ddot{c}_i(t) \int_0^l \phi_i(x)\phi_j(x)dx + \gamma \sum_{i=1}^{N} \dot{c}_i(t) \int_0^l \phi_i(x)\phi_j(x)dx +$$
$$c_d I \sum_{i=1}^{N} \dot{c}_i(t) \int_0^l \phi_i''(x)\phi_j(x)dx + I \sum_{i=1}^{N} c_i(t) \int_0^l \phi_i''(x)E(x)\phi_j(x)dx +$$
$$\dot{c}_i(t) \sum_{i=1}^{N} \int_0^l \int_0^l h(x,\xi)[\phi_i'(x) - \phi_i'(\xi)] d\xi \, \phi_j'(x) dx = 0. \quad (4.56)$$

This can be rewritten:

$$\rho A \begin{bmatrix} \ddot{c}_1(t) \\ ... \\ \ddot{c}_N(t) \end{bmatrix} \begin{bmatrix} \int_0^l \phi_1(x)\phi_1(x) & ... & \int_0^l \phi_1(x)\phi_N(x) \\ ... & ... & ... \\ \int_0^l \phi_N(x)\phi_1(x) & ... & \int_0^l \phi_N(x)\phi_N(x) \end{bmatrix} + \gamma \begin{bmatrix} \dot{c}_1(t) \\ ... \\ \dot{c}_N(t) \end{bmatrix} \quad (4.57)$$

$$\begin{bmatrix} \int_0^l \phi_1(x)\phi_1(x) & ... & \int_0^l \phi_1(x)\phi_N(x) \\ ... & ... & ... \\ \int_0^l \phi_N(x)\phi_1(x) & ... & \int_0^l \phi_N(x)\phi_N(x) \end{bmatrix} + \quad (4.58)$$

$$I \begin{bmatrix} c_1(t) \\ ... \\ c_N(t) \end{bmatrix} \begin{bmatrix} \int_0^l \phi_1''(x)\phi_1''(x)E(x) & ... & \int_0^l \phi_1''(x)\phi_N''(x)E(x) \\ ... & ... & ... \\ \int_0^l \phi_N''(x)\phi_1''(x)E(x) & ... & \int_0^l \phi_N''(x)\phi_N''(x)E(x) \end{bmatrix} \quad (4.59)$$

$$+c_d I \begin{bmatrix} \dot{c}_1(t) \\ ... \\ \dot{c}_N(t) \end{bmatrix} \begin{bmatrix} \int_0^l \phi_1''(x)\phi_1(x) & ... & \int_0^l \phi_1''(x)\phi_N(x) \\ ... & ... & ... \\ \int_0^l \phi_N(x)\phi_1(x) & ... & \int_0^l \phi_N(x)\phi_N(x) \end{bmatrix} \quad (4.60)$$

$$+\begin{bmatrix} \dot{c}_1(t) \\ \dots \\ \dot{c}_N(t) \end{bmatrix} \tag{4.61}$$

$$\begin{bmatrix} \int_0^l \int_0^l h(x,\xi)[\phi_1'(x)-\phi_1'(\xi)]d\xi\,\phi_1'(x)dx & \dots & \int_0^l \int_0^l h(x,\xi)[\phi_1'(x)-\phi_1'(\xi)]d\xi\,\phi_N'(x)dx \\ \dots & \dots & \dots \\ \int_0^l \int_0^l h(x,\xi)[\phi_N'(x)-\phi_N'(\xi)]d\xi\,\phi_1'(x)dx & \dots & \int_0^l \int_0^l h(x,\xi)[\phi_N'(x)-\phi_N'(\xi)]d\xi\,\phi_N'(x)dx \end{bmatrix} = 0 \tag{4.62}$$

Rewriting and grouping all like terms, we obtain the matrix system:

$$M\ddot{c}(t)+D\dot{c}(t)+Kc(t)=0 \tag{4.63}$$

The system matrices are defined as:

$$[M]_{i,j}=\rho A\int_0^l \phi_i(x)\phi_j(x)dx \tag{4.64}$$

$$[K]_{i,j}=I\int_0^l \phi_i''(x)\phi_j''(x)E(x)dx \tag{4.65}$$

$$[D]_{i,j}=\int_0^l \gamma\phi_i(x)\phi_j(x)dx+\int_0^l c_d I\phi_i''(x)\phi_j(x)dx+\int_0^l \Big[\int_0^l h(x,\xi)[\phi_i'(x)-\phi_i'(\xi)]d\xi\,\phi_j'(x)\Big]dx \tag{4.66}$$

This equation is then solved as in Section 4.1 of this chapter.

4.3 Morphing Wing Model

We are also interested in the application of such a model to a morphing-wing micro aerial vehicle. As such, we will examine the model for a wing in which the moment of inertia varies over the span of the wing. This model will also be approximated using the

generalized partial differential equation with free vibration:

$$\omega_{tt}(t,x)+L_1\omega_t(t,x)+L_2\omega(t,x)+\frac{\partial^2}{\partial x^2}\Big[\frac{EI(x)}{\rho A}\omega_{xx}(t,x)\Big]=0 \tag{4.67}$$

for $0 \leq x \leq l$ and $t \geq 0$ where the boundary conditions are:

$$\omega(t,0)=\frac{\partial \omega}{\partial x}(t,0)=0, \tag{4.68}$$

$$EI(l)\omega_{xx}(t,l)+c_dI(l)\omega_{xxt}(t,l)=0 \tag{4.69}$$

$$\frac{\partial}{\partial x}[EI(l)\omega_{xx}(t,x)+c_dI(l)\omega_{xxt}(t,x)]-\Big[\int_0^l h(x,\xi)(\omega_{xt}(t,x)-\omega_{xt}(t,\xi))d\xi\Big]=0 \tag{4.70}$$

where any simulation involving fewer forms of damping will use the boundary conditions outlined in Chapter 3.

Assuming all forms of damping, the beam model becomes:

$$\rho A\omega_{tt}(t,x)+\gamma\omega_t(t,x)+c_dI(x)\omega_{txxxx}(t,x)+EI_{xx}(x)\omega_{xx}(t,x)+$$
$$2EI_x(x)\omega_{xxx}(t,x)+EI(x)\omega_{xxxx}(t,x)-\frac{\partial}{\partial x}\Big[\int_0^l h(x,\xi)[\omega_{xt}(t,x)-\omega_{xt}(t,\xi)]d\xi\Big]=0 \tag{4.71}$$

4.3.1 Weak Formulation

The Galerkin Finite Element method is used once again to find numerical solutions to the Euler Bernoulli beam model. We multiply the beam equation by a test function $\phi(x)$ to obtain:

$$\rho A\omega_{tt}(t,x)\phi(x)+\gamma\omega_t(t,x)\phi(x)+c_dI(x)\omega_{txxxx}(t,x)\phi(x)+EI_{xx}(x)\omega_{xx}(t,x)\phi(x)$$
$$+2EI_x(x)\omega_{xxx}(t,x)\phi(x)+EI(x)\omega_{xxxx}(t,x)\phi(x)-$$
$$\frac{\partial}{\partial x}\Big[\int_0^l h(x,\xi)[\omega_{xt}(t,x)-\omega_{xt}(t,\xi)]d\xi\Big]\phi(x)=0 \tag{4.72}$$

Integrate with respect to x:

$$\int_0^l \rho A\omega_{tt}(t,x)\phi(x)dx+\int_0^l \gamma\omega_t(t,x)\phi(x)dx+\int_0^l c_d I(x)\omega_{txxxx}(t,x)\phi(x)dx+$$
$$\int_0^l EI(x)\omega_{xxxx}(t,x)\phi(x)dx+\int_0^l EI_{xx}(x)\omega_{xx}(t,x)\phi(x)dx+$$
$$\int_0^l 2EI_x(x)\omega_{xxx}(t,x)\phi(x)dx-\int_0^l \frac{\partial}{\partial x}\Big[\int_0^l h(x,\xi)[\omega_{xt}(t,x)-\omega_{xt}(t,\xi)]d\xi\Big]\phi(x)dx=0 \tag{4.73}$$

To make this a 2nd order partial differential equation, we need to integrate the 3rd term by parts:

$$\int_0^l c_d I(x)\omega_{txxxx}(t,x)\phi(x)dx = c_d I(x)\omega_{txxx}(t,x)\phi(x)|_0^L-\int_0^l c_d I_x(x)\omega_{txxx}(t,x)\phi(x)dx$$
$$-\int_0^l c_d I(x)\omega_{txxx}(t,x)\phi_x(x)dx \tag{4.74}$$

And applying integration by parts again to the 2nd and 3rd terms:

$$\int_0^l c_d I_x(x)\omega_{txxx}(t,x)\phi(x)dx = c_d I_x(x)\omega_{txx}(t,x)\phi(x)|_0^l-\int_0^l c_d I_{xx}(x)\omega_{txx}(t,x)\phi(x)dx$$
$$-\int_0^l c_d I_x(x)\omega_{txx}(t,x)\phi_x(x)dx \tag{4.75}$$

And,

$$\int_0^l c_d I(x)\omega_{txxx}(t,x)\phi_x(x)dx = c_d I(x)\omega_{txx}(t,x)\phi_x(x)|_0^l-\int_0^l c_d I_x(x)\omega_{txx}(t,x)\phi_x(x)dx$$
$$-\int_0^l c_d I(x)\omega_{txx}(t,x)\phi_{xx}(x)dx \tag{4.76}$$

So:

$$\int_0^l c_d I(x)\omega_{txxxx}(t,x)\phi(x)dx = c_d I(x)\omega_{txxx}(t,x)\phi(x)|_0^l+$$
$$c_d I_x(x)\omega_{txx}(t,x)\phi(x)|_0^l+\int_0^l c_d I_{xx}(x)\omega_{txx}(t,x)\phi(x)dx$$

$$+\int_0^l c_d I_x(x)\omega_{txx}(t,x)\phi_x(x)dx - c_d I(x)\omega_{txx}(t,x)\phi_x(x)|_0^l$$
$$+\int_0^l c_d I_x(x)\omega_{txx}(t,x)\phi_x(x)dx + \int_0^l c_d I(x)\omega_{txx}(t,x)\phi_{xx}(x)dx \quad (4.77)$$

Likewise, we integrate the 4th term by parts:

$$\int_0^l EI(x)\omega_{xxxx}(t,x)\phi(x)dx = EI(x)\omega_{xxx}(t,x)\phi(x)|_0^l - \int_0^l EI_x(x)\omega_{xxx}(t,x)\phi(x)dx -$$
$$\int_0^l EI(x)\omega_{xxx}(t,x)\phi_x(x)dx \quad (4.78)$$

And applying integration by parts again (first, to the second term and then to the third term):

$$\int_0^l EI_x(x)\omega_{xxx}(t,x)\phi(x)dx = EI_x(x)\omega_{xx}(t,x)\phi(x)|_0^l - \int_0^l EI_{xx}(x)\omega_{xx}(t,x)\phi(x)dx -$$
$$\int_0^l EI_x(x)\omega_{xx}(t,x)\phi_x(x)dx \quad (4.79)$$

And,

$$\int_0^l EI(x)\omega_{xxx}(t,x)\phi_x(x)dx = EI(x)\omega_{xx}(t,x)\phi_x(x)|_0^l - \int_0^l EI_x(x)\omega_{xx}(t,x)\phi_x(x)dx -$$
$$\int_0^l EI(x)\omega_{xx}(t,x)\phi_{xx}(x)dx \quad (4.80)$$

So:

$$\int_0^l EI(x)\omega_{xxxx}(t,x)\phi(x)dx = EI(x)\omega_{xxx}(t,x)\phi(x)|_0^l - EI_x(x)\omega_{xx}(t,x)\phi(x)|_0^l +$$
$$\int_0^l EI_{xx}(x)\omega_{xx}(t,x)\phi(x)dx + \int_0^l EI_x(x)\omega_{xx}(t,x)\phi_x(x)dx - EI(x)\omega_{xx}(t,x)\phi_x(x)|_0^l$$
$$+\int_0^l EI_x(x)\omega_{xx}(t,x)\phi_x(x)dx + \int_0^l EI(x)\omega_{xx}(t,x)\phi_{xx}(x)dx \quad (4.81)$$

Lastly:

$$\int_0^l 2EI_x(x)\omega_{xxx}(t,x)\phi(x)dx = 2EI_x(x)\omega_{xx}(t,x)\phi(x)\Big|_0^l - 2\int_0^l EI_{xx}(x)\omega_{xx}(t,x)\phi(x)dx -$$
$$2\int_0^l EI_x(x)\omega_{xx}(t,x)\phi_x(x)dx \quad (4.82)$$

In order to apply the boundary conditions, we are also going to integrate the spatial hysteresis term by parts, as before. The weak form is now:

$$\int_0^l \rho A\omega_{tt}(t,x)\phi(x)dx+\int_0^l \gamma\omega_t(t,x)\phi(x)dx+c_dI(l)\omega_{txxx}(t,l)\phi(l)$$
$$-c_dI_x(l)\omega_{txx}(t,l)\phi(l)+c_dI(l)\omega_{txx}(t,l)\phi_x(l)+\int_0^l c_dI_{xx}(x)\omega_{txx}(t,x)\phi(x)dx$$
$$+2EI_x(x)\omega_{xx}(t,x)\phi(x)\Big|_0^l-\int_0^l EI_{xx}(x)\omega_{xx}(t,x)\phi(x)dx-\int_0^l EI_x(x)\omega_{xx}(t,x)\phi_x(x)dx$$
$$+2\int_0^l c_dI_x(x)\omega_{txx}(t,x)\phi_x(x)dx+\int_0^l c_dI(x)\omega_{txx}(t,x)\phi_{xx}(x)dx+$$
$$EI(l)\omega_{xxx}(t,l)\phi(l)-EI_x(l)\omega_{xx}(t,l)\phi(l)-EI(l)\omega_{xx}(t,l)\phi_x(l)+$$
$$\int_0^l EI_{xx}(x)\omega_{xx}(t,x)\phi(x)dx+\int_0^l EI_{xx}(x)\omega_{xx}(t,x)\phi(x)dx+2\int_0^l EI_x(x)\omega_{xx}(t,x)\phi_x(x)dx+$$
$$\int_0^l EI(x)\omega_{xx}(t,x)\phi_{xx}(x)dx-\phi_x(x)\int_0^l h(x,\xi)[\omega_{xt}(t,x)-\omega_{xt}(t,\xi)]d\xi\,|_0^l+$$
$$\int_0^l\Big[\int_0^l h(x,\xi)[\omega_{xt}(t,x)-\omega_{xt}(t,\xi)]d\xi\Big]\phi(x)dx=0 \quad (4.83)$$

Apply the appropriate boundary conditions and we have:

$$\int_0^l \rho A\omega_{tt}(t,x)\phi(x)dx+\int_0^l \gamma\omega_t(t,x)\phi(x)dx+\int_0^l c_dI_{xx}(x)\omega_{txx}(t,x)\phi(x)dx$$
$$+2\int_0^l c_dI_x(x)\omega_{txx}(t,x)\phi_x(x)dx+\int_0^l c_dI(x)\omega_{txx}(t,x)\phi_{xx}(x)dx+$$
$$\int_0^l EI(x)\omega_{xx}(t,x)\phi_{xx}(x)dx+\int_0^l\Big[\int_0^l h(x,\xi)[\omega_{xt}(t,x)-\omega_{xt}(t,\xi)]d\xi\Big]\phi(x)dx=0 \quad (4.84)$$

4.3.2 Cubic Hermitian Polynomials

Now that we have found the weak form of the equation, we are able to approximate the displacement of the beam using cubic Hermite polynomials. This method divides the beam into N subintervals:

$$\omega(t,x)\cong\omega^N(t,s)=\sum_{i=1}^N c_i(t)\phi_i(x), \quad (4.85)$$

where $\phi_i(x)$ are the spatially dependent cubic spline basis functions and $c_i(t)$ are the time dependent coefficients.

Substituting (4.85) into (4.84), we get the equation:

$$\int_0^l \rho A \sum_{i=1}^{N} \ddot{c}_i(t)\phi_i(x)\phi(x)dx + \int_0^l \gamma \sum_{i=1}^{N} \dot{c}_i(t)\phi_i(x)\phi(x)dx + \int_0^l c_d \sum_{i=1}^{N} \dot{c}_i(t)\phi_i''(x)I''(x)\phi(x)dx + 2\int_0^l c_d \sum_{i=1}^{N} \dot{c}_i(t)\phi_i''(x)I'(x)\phi'(x)dx + \int_0^l c_d \sum_{i=1}^{N} \dot{c}_i(t)\phi_i''(x)I(x)\phi''(x)dx + \int_0^l E \sum_{i=1}^{N} c_i(t)\phi_i''(x)I(x)\phi''(x)dx + \int_0^l \Big[\int_0^l h(x,\xi) \sum_{i=1}^{N} [\dot{c}_i(t)\phi_i'(x) - \dot{c}_i(t)\phi_i'(\xi)]d\xi \Big] \phi'(x)dx = 0. \quad (4.86)$$

where $\dot{c} = c_t$ and $\phi' = \phi_x$. Choosing a function $\phi(x)$ with a range over the basis function of $\phi_j(x)$ for $j = 1,2,...,N$ and simplifying:

$$\rho A \sum_{i=1}^{N} \ddot{c}_i(t) \int_0^l \phi_i(x)\phi_j(x)dx + \gamma \sum_{i=1}^{N} \dot{c}_i(t) \int_0^l \phi_i(x)\phi_j(x)dx + c_d \sum_{i=1}^{N} \dot{c}_i(t) \int_0^l \phi_i''(x)I''(x)\phi_j(x)dx + 2c_d \sum_{i=1}^{N} \dot{c}_i(t) \int_0^l \phi_i''(x)I'(x)\phi_j'(x)dx + c_d \sum_{i=1}^{N} \dot{c}_i(t) \int_0^l \phi_i''(x)I(x)\phi_j'(x)dx + E \sum_{i=1}^{N} c_i(t) \int_0^l \phi_i''(x)I(x)\phi_j''(x)dx + \dot{c}_i(t) \sum_{i=1}^{N} \int_0^l \int_0^l h(x,\xi)[\phi_i'(x) - \phi_i'(\xi)]d\xi\, \phi_j'(x)dx = 0. \quad (4.87)$$

This can be rewritten:

$$\rho A \begin{bmatrix} \ddot{c}_1(t) \\ ... \\ \ddot{c}_N(t) \end{bmatrix} \begin{bmatrix} \int_0^l \phi_1(x)\phi_1(x) & ... & \int_0^l \phi_1(x)\phi_N(x) \\ ... & ... & ... \\ \int_0^l \phi_N(x)\phi_1(x) & ... & \int_0^l \phi_N(x)\phi_N(x) \end{bmatrix} + \gamma \begin{bmatrix} \dot{c}_1(t) \\ ... \\ \dot{c}_N(t) \end{bmatrix} \quad (4.88)$$

$$\begin{bmatrix} \int_0^l \phi_1(x)\phi_1(x) & \dots & \int_0^l \phi_1(x)\phi_N(x) \\ \dots & \dots & \dots \\ \int_0^l \phi_N(x)\phi_1(x) & \dots & \int_0^l \phi_N(x)\phi_N(x) \end{bmatrix} + \tag{4.89}$$

$$E \begin{bmatrix} c_1(t) \\ \dots \\ c_N(t) \end{bmatrix} \begin{bmatrix} \int_0^l \phi_1''(x)\phi_1''(x)I(x) & \dots & \int_0^l \phi_1''(x)\phi_N''(x)I(x) \\ \dots & \dots & \dots \\ \int_0^l \phi_N''(x)\phi_1''(x)I(x) & \dots & \int_0^l \phi_N''(x)\phi_N''(x)I(x) \end{bmatrix} \tag{4.90}$$

$$+c_d \begin{bmatrix} \dot{c}_1(t) \\ \dots \\ \dot{c}_N(t) \end{bmatrix} \begin{bmatrix} \dots & \dots & \int_0^l \phi_1''(x)\phi_N(x)I''(x) + 2\int_0^l \phi_1''(x)\phi_N'(x)I'(x) + \int_0^l \phi_1''(x)\phi_N''(x)I(x) \\ \dots & \dots & \dots \\ \dots & \dots & \int_0^l \phi_N(x)\phi_N(x)I''(x) + 2\int_0^l \phi_N''(x)\phi_N'(x)I'(x) + \int_0^l \phi_N''(x)\phi_N''(x)I(x) \end{bmatrix} \tag{4.91}$$

$$+ \begin{bmatrix} \dot{c}_1(t) \\ \dots \\ \dot{c}_N(t) \end{bmatrix} \tag{4.92}$$

$$\begin{bmatrix} \int_0^l \int_0^l h(x,\xi)[\phi_1'(x) - \phi_1'(\xi)]d\xi\,\phi_1'(x)dx & \dots & \int_0^l \int_0^l h(x,\xi)[\phi_1'(x) - \phi_1'(\xi)]d\xi\,\phi_N'(x)dx \\ \dots & \dots & \dots \\ \int_0^l \int_0^l h(x,\xi)[\phi_N'(x) - \phi_N'(\xi)]d\xi\,\phi_1'(x)dx & \dots & \int_0^l \int_0^l h(x,\xi)[\phi_N'(x) - \phi_N'(\xi)]d\xi\,\phi_N'(x)dx \end{bmatrix} = 0 \tag{4.93}$$

Rewriting and grouping all like terms, we obtain the matrix system:

$$M\ddot{c}(t) + D\dot{c}(t) + Kc(t) = 0 \tag{4.94}$$

The system matrices are defined as:

$$[M]_{i,j} = \rho A \int_0^l \phi_i(x)\phi_j(x)dx \tag{4.95}$$

$$[K]_{i,j} = E\int_0^l \phi_i''(x)\phi_j''(x)I(x)dx \tag{4.96}$$

$$[D]_{i,j} = \int_0^l \gamma\phi_i(x)\phi_j(x)dx + c_d\int_0^l \phi_i''(x)\phi_j(x)I''(x)dx + 2c_d\int_0^l \phi_i''(x)\phi_j'(x)I'(x)dx + c_d\int_0^l \phi_i''(x)\phi_j''(x)I(x)dx + \int_0^l \Big[\int_0^l h(x,\xi)[\phi_i'(x) - \phi_i'(\xi)]d\xi\,\phi_j'(x)\Big]dx \tag{4.97}$$

This equation is then solved as in Section 4.1 of this chapter.

CHAPTER 5

EXPERIMENTAL SETUP

Since the focus of the dissertation is flexible-wing UAVs, we wanted to construct our own wing for such a model. The University of Florida has several guides on how to assemble flexible, composite parts so we used the process outlined in those [1], [4]. Throughout this work, we are assuming dimensions consistent with that of a micro aerial vehicle. As such, the beam parameters are similar to those found on such aircrafts. The composite beam was cut out of a woven carbon fiber sheet. This carbon fiber sheet was pre-treated with thermoset epoxy and was constructed in a plain weave, bi-directional orientation. This was then covered with a latex membrane to mimic an elastic, morphable, flexible, composite wing.

5.1 Beam Construction

The first stage of construction was a standard manufacturing process. The structure was measured and cut. In order to construct the beam, we chose to design each beam as one foot long and 5 inches wide. These dimensions seem appropriate given that we are interested in the applications for mid-sized MAVs. The height was determined by how many layers of carbon fiber fabric and epoxy were used.

5.1.1 Materials

In order to construct the beam, the following material were used:

- Carbon Fiber Sheets: 24” x 24”
- Fast Dry Epoxy Resin: 1 gallon
- Epoxy Hardener: 1/2 gallon
- Roll of Nylon Bagging Film
- Roll of Peel Ply Release Film
- Sealant Tape
- Roll of Bleeder Cloth
- Metal Shears
- Gasket
- Bike Pump

5.1.2 Beam Structure

Cutting the carbon fiber was a non-trivial process. First, the dimensions were measured and carefully marked. Then, the outside of the beam was cut and sanded down until the structure was uniform. Last, all the interior holes were cut in the beam using metal shears and hand sanded until they were uniform. These interior sections were cut out of each beam in order to make the beam more flexible and consistent with the material of a MAV wing. These sections are 4 inches wide and 3 inches long and are spaced uniformly along the beam. Once a single wing was cut, a total of 5 more identical beams were cut in order to create both double and triple layered beams.

5.2 Vacuum Bagging

In order to attach multiple layers of carbon fiber together, a process called vacuum bagging was used. Vacuum bagging is a process which uses atmospheric pressure to create uniform pressure along a surface while it cures [4], [1]. This serves several purposes. It removes excess air between the layers, compacts the fiber layers together to create a more uniform material, and optimizes the fiber-to-resin ratio. Optimizing the fiber-to-resin ratio is important in a MAV wing construction. Before reinforcement, the carbon fiber is flexible, while the epoxy resin is very brittle. We want to use enough resin to completely bond the material, but not too much as to create a brittle structure. The steps for vacuum bagging are outlined in the next few paragraphs.

First, the vacuum bagging sealed bag was created. Since vacuum bagging uses a vacuum to create a pressure differential with the atmosphere, it is important that the bag is sealed without any leakage. The bag was created out of thick bagging plastic. The bag needed to be large enough to contain the beam, peel ply, and breather cloth. In order to construct it, the sheet of plastic was taped down to maintain tension and sealing tape was applied to the two sides and mouth of the bag, as shown in Figure 5.1.

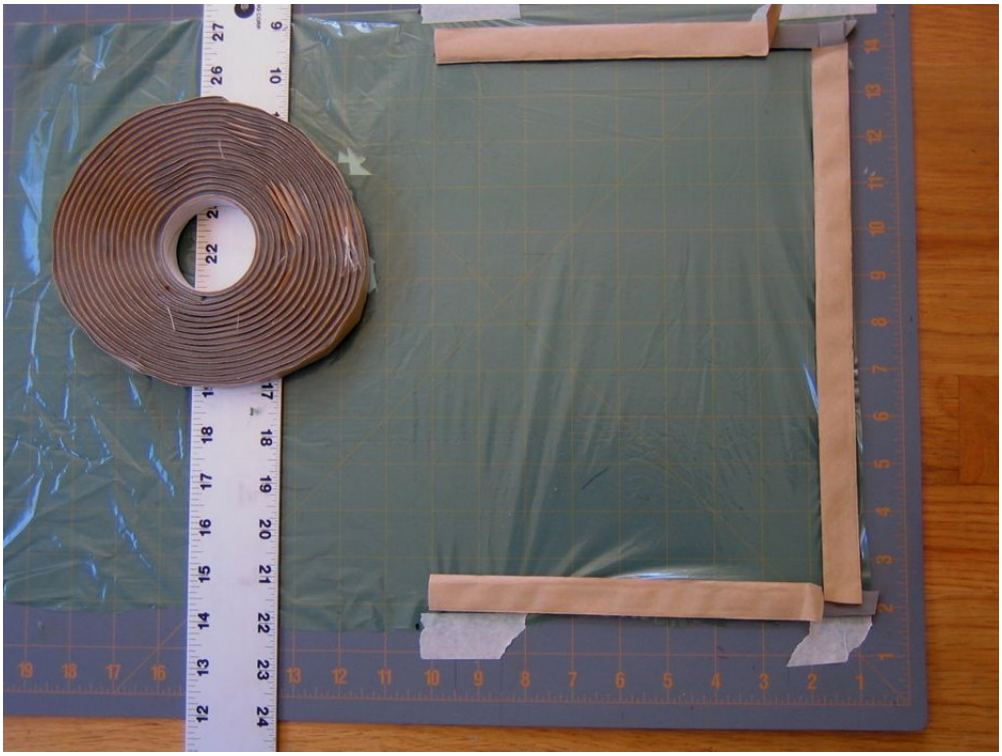

Figure 5.1: Vacuum Bag Construction

The two pieces of tape on the side of the bag were peeled back slowly and pressure was applied to the top layer on each side, one at a time. Once the two sides were sealed, a bag-tube adapter was inserted. To create this, a hole was cut in the bag, then a gasket and nut were placed through the hole. This provides a place to connect the vacuum pump while still providing a seal. This is pictured in Figure 5.2.

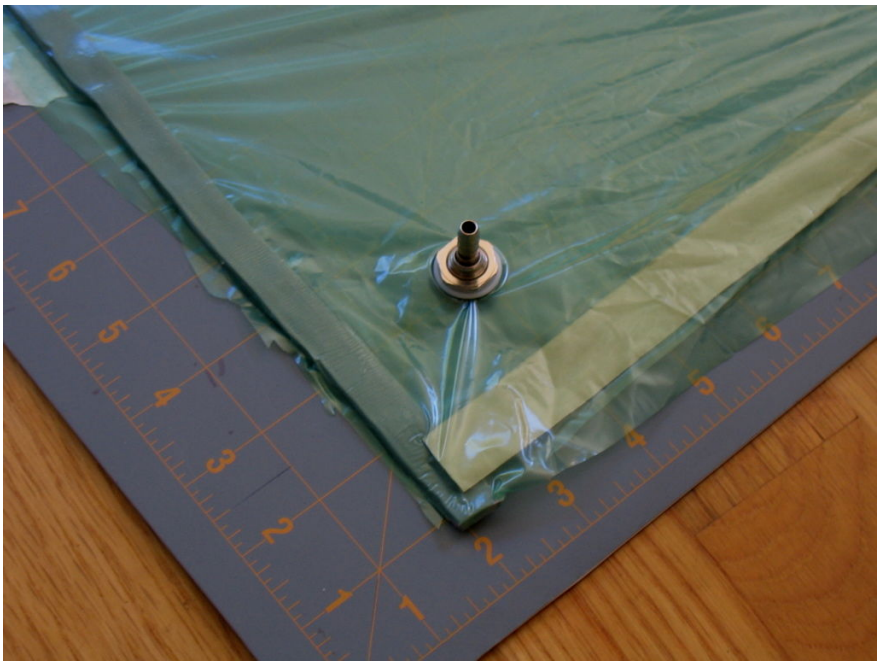

Figure 5.2: Vacuum Bag Construction 2

Second, a homemade vacuum was manufactured. In order to do this, I took a bike pump and converted it to suck air out of the bag. Since a bike pump is created to pump air into an object rather than removing it, two changes had to be made to the bike pump. First, the piston and metals discs had to be reversed. Second, the check valve needed to be reversed. This was a relatively straight forward project in which I was able to create a vacuum out of supplies I already had.

Now, the beam had to be prepared for curing. An epoxy resin was mixed with an emulsifier then painted onto the surface of the carbon fiber sheet. The two layers were layered together. Peel ply was wrapped around the entire beam to prevent the beam from curing to the bagging materials. Then the whole beam was wrapped in bleeder cloth to absorb extra epoxy. The part was placed in the vacuum bag as shown in Figure 5.3.

Figure 5.3: Final Curing

The last step of the carbon fiber frame construction was the curing process itself. The bag was sealed, all excess air was extracted, and the part was left in the bag overnight. Once cured overnight, all extra residue was removed by sanding. This completed the construction of the carbon fiber skeleton of the MAV wing.

5.3 Affixing the Membrane

Likewise, affixing latex to the frame was a tedious process. Latex is difficult to attach because it is prone to bubbles and other structural inconsistencies. In order to overcome this, a large amount of uniform pretension was applied to the latex [1]. The difference in results can be seen on the balsa wood model pictured in Figure 5.4.

Figure 5.4: Effects of Applying Pretension to Latex

Uniform pretension was applied by clipping the outside edges of the latex to a large piece of particle board, placing the carbon fiber frame and glue on top, and allowing the frame to dry before removing the clips. That way, when the adhesive dried, the latex did not lose its tension.

The final beam is a result of all the processes described throughout this chapter. It can be seen in Figure 5.5 and Figure 5.6. A total of three beams, each with a different number of carbon fiber layers, were constructed for this project.

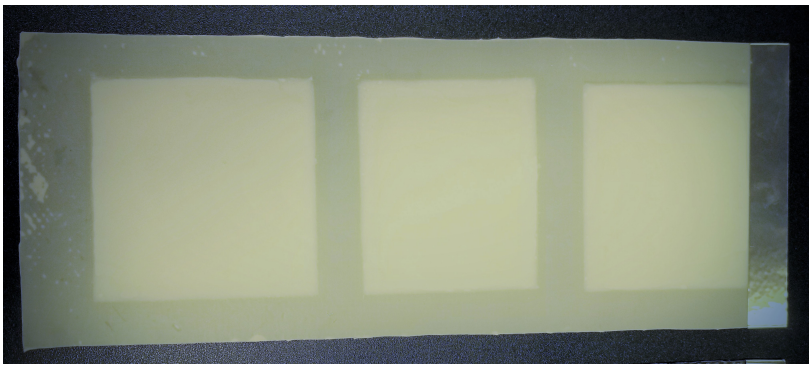

Figure 5.5: Final Beam Front

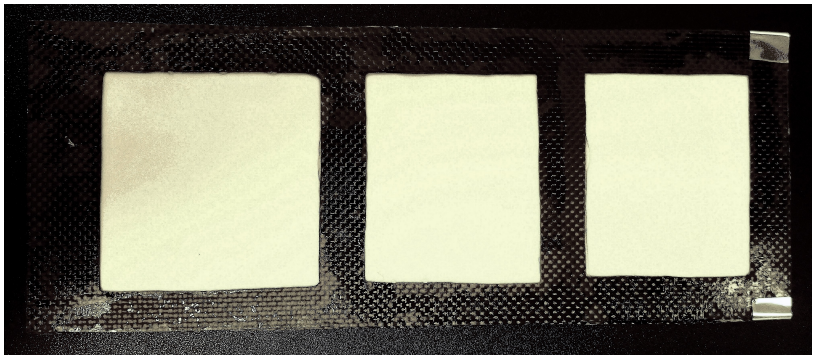

Figure 5.6: Final Beam Back

5.4 Vibrational Analysis

The experiment was run using all three beams and a cantilevered beam setup. The composite beam was cantilevered by clamping the beam on top of a 1” square rod and the table using a metal vice. A strip of mirrored tape was placed at the tip of each beam to better reflect the light off the surface. Then, a laser vibrometer was pointed at this tape. The setup is seen in Figure 5.7 and Figure 5.8.

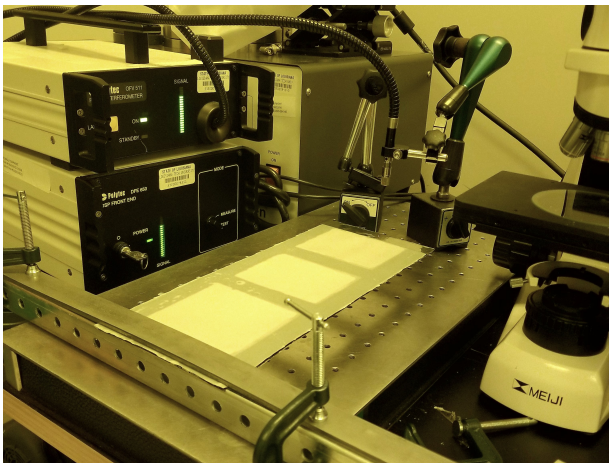

Figure 5.7: Cantilever Beam Setup

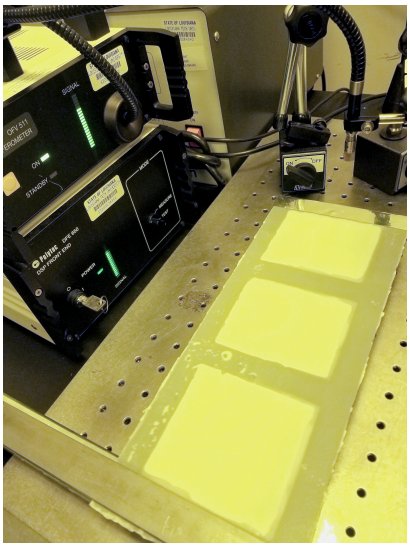

Figure 5.8: Cantilever Beam Setup 2

The actual vibrometer used was a Polytec OFV 511. This vibrometer is used for taking measurements without making contact with the beam. Since we are dealing with light, flexible beams, this is imperative. A contact measurement would significantly alter the vibrational results. Thus, no contact measurements were taken. Using this laser vibrometer,

the laser is reflected off a shiny surface at the beam tip and the light signal is compared to the initial signal to gauge the displacement or velocity of the beam.

To collect data, each beam was excited with an impact hammer for five different trials. The impact hammer output a force reading. And, the laser vibrometer analyzer collected displacement data. This displacement data was recorded and used in the inverse parameter estimation to be analyzed for the different damping models.

CHAPTER 6

EXPERIMENTAL RESULTS

6.1 Single Layered Cantilevered Beam

The first beam which was analyzed was a single ply of carbon fiber fabric with a latex membrane. The beam dimensions can be found in Table 6.1:

Table 6.1: Single Beam Parameters

Parameter	Value	Units
Length	0.3048	Meters
Width	0.127	Meters
Height	0.00072	Meters
Mass	0.021	Kilograms

6.1.1 Initial Measurement Plots

The tip displacement was measured over a period of five seconds at 0.003906 second intervals. Five trials were run, each with a slightly different input force. The results from this measurement can be seen in Figure 6.1.

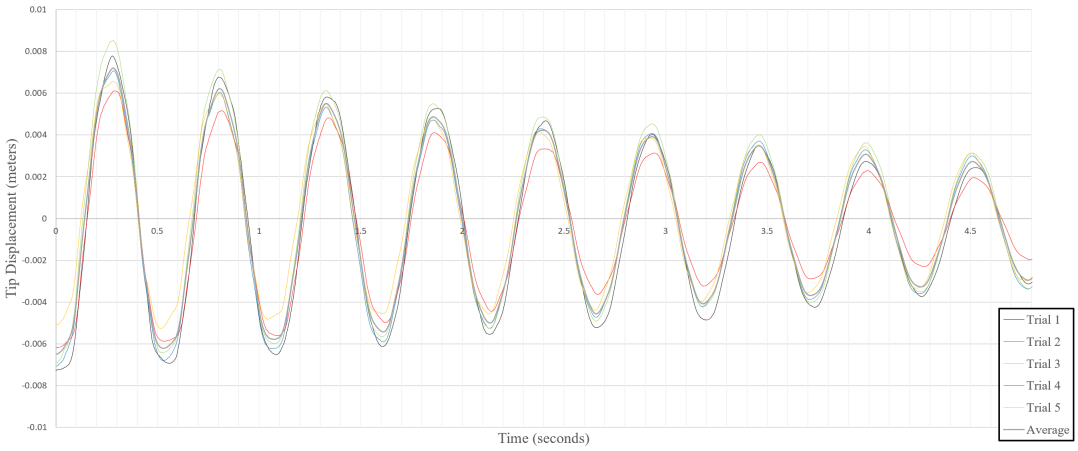

Figure 6.1: Single Ply Cantilevered Beam Results

This is a flexible beam, so it has a long period of oscillation and dampens relatively slowly. As we would expect given we are using an identical beam in each trial, the period remains nearly identical in the five trials. The only noticeable difference between the trials are the amplitudes, which are the result of differing impact forces.

6.1.2 Simulation Results

After this tip data was collected, the inverse parameter estimation was run for each of the trials. These values were then substituted back into the beam equation to compare the simulated data to the experimental data. The results from each of these trials is seen below.

Trial One

Trial 1 was subjected to an initial force $6.05 \times 10^{-5} N$. When the inverse parameter estimation was run for each of the models, it converged at the values seen in Table 6.2

Table 6.2: Damping Parameter Values for Single Beam Trial 1

	$E\left(\frac{N}{m^2}\right)$	$\gamma\left(\frac{kg}{m}\right)$	$c_d\left(\frac{kg}{m}\right)$	a	b
Viscous	6.172×10^8	0.4972	N/A	N/A	N/A
Viscous/KV	6.167×10^7	0.0162	9.480×10^4	N/A	N/A
Viscous/SH	6.174×10^7	0.0209	N/A	5.639×10^{-5}	6.936×10^{-4}

These values were substituted into the beam equation so the simulated data could be compared to the experimental data. The comparison of all three models then is seen in Figure 6.2.

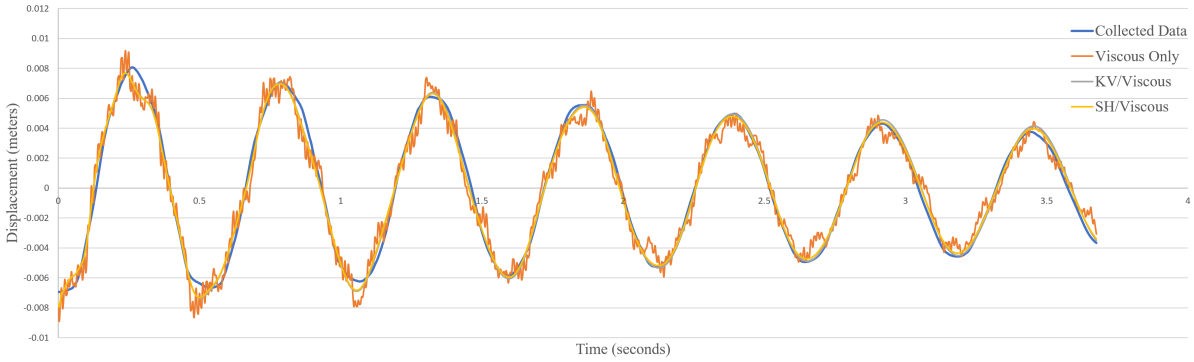

Figure 6.2: Tip Vibration for Single Ply Beam Trial 1

All simulations were modeled using the vibrational analysis data. As such, there is some noise present in the model. This most likely arises from the uncertainty in the initial conditions vector. The laser vibrometer is accurate to .01 mm. Additionally, some error and uncertainty propagates throughout the model from inaccuracy in the length measurements. All beam construction was done by hand, so the accuracy can only be guaranteed to approximately 1 mm. This introduces some error as a result of construction limitations.

This is most noticeable in the viscous damping model as the damping coefficient is directly proportional to the tip displacement data. Additionally, at low frequencies, structural noise is present in a cantilevered beam model since the initial conditions were not computed at a natural frequency or mode so we see the interaction of several modes in the vibration data. These sources of error are mentioned only to explain any deviations from a smooth, continuous tip displacement plot and will not affect the comparison of the different damping models.

The performance was then analyzed for each model where the error was calculated using the cost equation described in the previous section as:

$$J^N(q) = \sum_{i=1}^{M} |\omega^N(t,l,q) - \hat{\omega}(t,l)|^2 \tag{6.1}$$

where $\omega(t,x,q)$ denotes a solution with the appropriate boundary and initial conditions based on the parameter values and M is the number of tip displacement measurements.

The total error can be used to find the average error by dividing the total error by the number of trials:

$$\sigma_J = \frac{\sum_{i=1}^{M} |\omega^N(t,l,q) - \hat{\omega}(t,l)|^2}{M}. \tag{6.2}$$

For the three models these values were:

1. Viscous Damping:
   - Total Error: 0.60789 m
   - Average Error: 0.00064 m
   - Percent Error: 17.34%
2. Viscous and Kelvin Voigt Damping:
   - Total Error: 0.28247 m

- Average Error: 0.00030 m
- Percent Error: 8.06%

3. Viscous and Spatial Hysteresis Damping:
   - Total Error: 0.22685 m
   - Average Error: 0.00024 m
   - Percent Error: 6.47%

This process was then repeated for each of the five trials.

Trials Two - Five

Because the same process was repeated 4 more times, the results have been condensed in the following pages. The initial force for trials 2-5 were

$[6.03 \times 10^{-5}, 6.10 \times 10^{-5}, 5.10 \times 10^{-5}, 4.60 \times 10^{-5}]$ newtons respectively. The values for the damping parameters can be found in Table 6.3, Table 6.4, Table 6.5, and Table 6.6.

Table 6.3: Damping Parameter Values for Single Ply Beam Trial 2

	$E\left(\frac{N}{m^2}\right)$	$\gamma\left(\frac{kg}{m}\right)$	$c_d\left(\frac{kg}{m}\right)$	a	b
Viscous	6.221×10^8	0.4712	N/A	N/A	N/A
Viscous/KV	6.233×10^7	0.0168	9.132×10^4	N/A	N/A
Viscous/SH	6.219×10^7	0.0157	N/A	6.128×10^{-5}	7.10×10^{-4}

Table 6.4: Damping Parameter Values for Single Ply Beam Trial 3

	$E\left(\frac{N}{m^2}\right)$	$\gamma\left(\frac{kg}{m}\right)$	$c_d\left(\frac{kg}{m}\right)$	a	b
Viscous	6.227×10^8	0.5619	N/A	N/A	N/A
Viscous/KV	6.216×10^7	0.0204	9.109×10^4	N/A	N/A
Viscous/SH	6.227×10^7	0.0192	N/A	6.239×10^{-5}	6.999×10^{-4}

Table 6.5: Damping Parameter Values for Single Ply Beam Trial 4

	$E\left(\frac{N}{m^2}\right)$	$\gamma\left(\frac{kg}{m}\right)$	$c_d\left(\frac{kg}{m}\right)$	a	b
Viscous	6.190×10^8	0.6022	N/A	N/A	N/A
Viscous/KV	6.179×10^7	0.0264	9.212×10^4	N/A	N/A
Viscous/SH	6.181×10^7	0.0236	N/A	6.310×10^{-5}	7.010×10^{-4}

Table 6.6: Damping Parameter Values for Single Ply Beam Trial 5

	$E\frac{N}{m^2}$	$\gamma\frac{kg}{m}$	$c_d\frac{kg}{m}$	a	b
Viscous	6.249×10^8	0.4121	N/A	N/A	N/A
Viscous/KV	6.260×10^7	0.0154	9.227×10^4	N/A	N/A
Viscous/SH	6.281×10^7	0.0147	N/A	6.292×10^{-5}	7.109×10^{-4}

These values were substituted into the beam equation so the simulated data could be compared to the experimental data. Each of the trials have been plotted in Figure 6.3, Figure 6.4, Figure 6.5, and Figure 6.6.

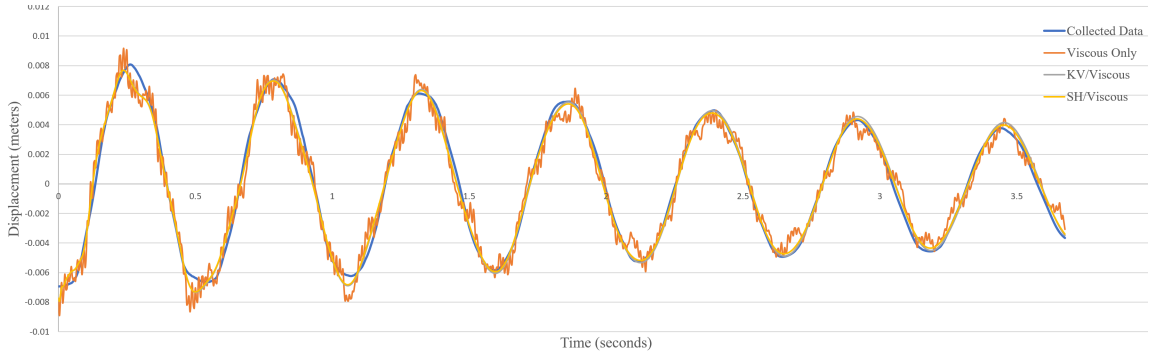

Figure 6.3: Tip Vibration for Single Ply Beam Trial 2

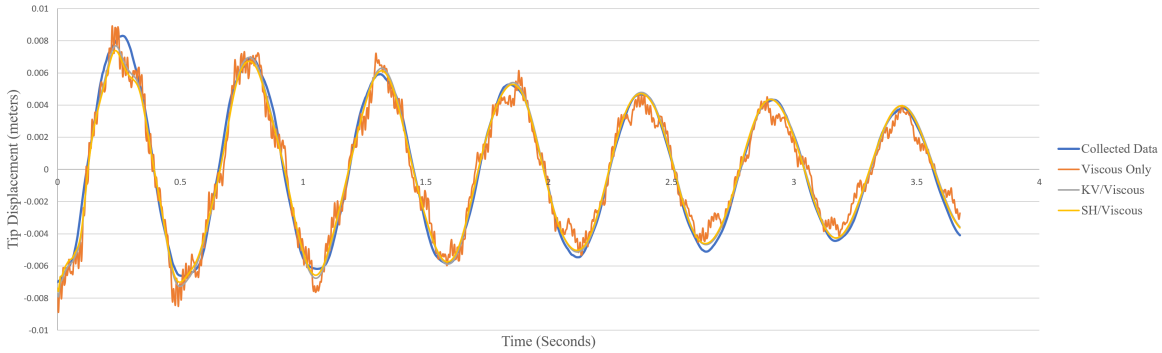

Figure 6.4: Tip Vibration for Single Ply Beam Trial 3

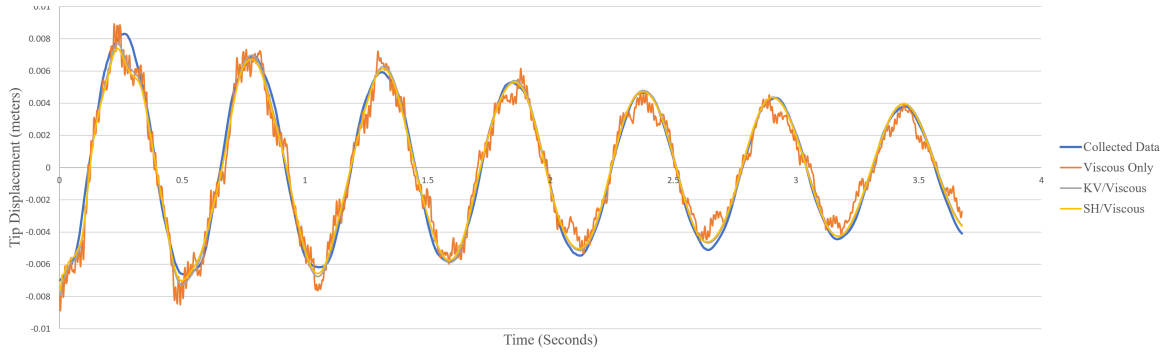

Figure 6.5: Tip Vibration for Single Ply Beam Trial 4

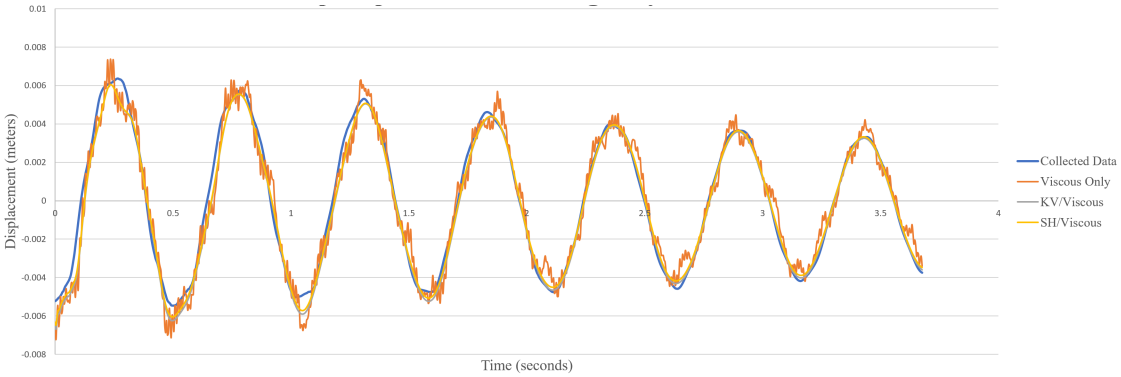

Figure 6.6: Tip Vibration for Single Ply Beam Trial 5

Using the same method as before, the error was calculated for each trial and the values can be seen in Table 6.7, Table 6.8, Table 6.9, and Table 6.10.

Table 6.7: Error for Single Ply Beam Trial 2

	Total Error	Average Error	Percent Error
Viscous	0.533372 m	0.000566 m	16.54%
Viscous/KV	0.207257 m	0.000220 m	6.43%
Viscous/SH	0.171137 m	0.000182 m	5.31%

Table 6.8: Error for Single Ply Beam Trial 3

	Total Error	Average Error	Percent Error
Viscous	0.643658 m	0.000683 m	18.59%
Viscous/KV	0.251340 m	0.000267 m	7.26%
Viscous/SH	0.207897 m	0.000221 m	6.01%

Table 6.9: Error for Single Ply Beam Trial 4

	Total Error	Average Error	Percent Error
Viscous	0.521681 m	0.000554 m	18.94%
Viscous/KV	0.286249 m	0.000304 m	10.39%
Viscous/SH	0.246603 m	0.000262 m	8.95%

Table 6.10: Error for Single Ply Beam Trial 5

	Total Error	Average Error	Percent Error
Viscous	0.548491 m	0.000582 m	18.87%
Viscous/KV	0.312577 m	0.000332 m	10.76%
Viscous/SH	0.216658 m	0.000230 m	7.46%

6.1.3 Modal Analysis

Traditional modal analysis is commonly used to estimate the modulus of elasticity. During free vibration, there in no energy input into the system. Since we are modeling the impact as a single impulse, this beam is freely vibrating after impact. Since we have a measurement for the impact force and displacement data at the tip of the beam, we can use the beam deflection equation to roughly approximate the modulus of elasticity where δ is the displacement of the beam tip and P is the applied force at $t = 0$ [14].

$$\delta = \frac{PL^3}{3EI} \tag{6.3}$$

We can rearrange this equation as:

$$E = \frac{PL^3}{3\delta I} \tag{6.4}$$

For each of the five trials, this value is:

$$E_1 = \frac{(6.05 \times 10^{-5} N)(.3048m)^3}{3(0.00695m)\frac{.127m(.00072m^3)}{12}} = 6.24 \times 10^7 \frac{N}{m^2} \tag{6.5}$$

$$E_2 = \frac{(6.03 \times 10^{-5} N)(.3048m)^3}{3(0.00695m)\frac{.127m(.00072m^3)}{12}} = 6.22 \times 10^7 \frac{N}{m^2} \tag{6.6}$$

$$E_3 = \frac{(6.10 \times 10^{-5} N)(.3048m)^3}{3(0.00699m)\frac{.127m(.00072m^3)}{12}} = 6.25 \times 10^7 \frac{N}{m^2} \tag{6.7}$$

$$E_4 = \frac{(5.10 \times 10^{-5} N)(.3048m)^3}{3(0.00589m)\frac{.127m(.00072m^3)}{12}} = 6.20 \times 10^7 \frac{N}{m^2} \tag{6.8}$$

$$E_5 = \frac{(4.60 \times 10^{-5} N)(.3048m)^3}{3(0.00524m)\frac{.127m(.00072m^3)}{12}} = 6.29 \times 10^7 \frac{N}{m^2} \tag{6.9}$$

Where the average modulus of elasticity is then calculated as:

$$E = \frac{\sum_{i=1}^{5} E_i}{5} = 6.24 \times 10^7 \frac{N}{m^2} \tag{6.10}$$

And, the standard deviation is:

$$\sigma^2 = \frac{\sum E_i - E}{5} = 0.30 \times 10^7 \frac{N}{m^2} \tag{6.11}$$

This is included to validate that the results obtained throughout the paper are within an appropriate range of the value obtained through a commonly accepted method. Traditional modal analysis is not used in this project because it cannot be used to solve all the beam parameters as it does not work with the hysteresis terms or with spatially dependent parameters. However, it can be used to roughly calculate the modulus of elasticity at the cantilevered beam tip, which is in good agreement with both models.

6.1.4 Summary of Results

The first model used only external, viscous damping. The estimated parameters then are $q = [E, \gamma]$ where E is the modulus of elasticity and γ is the viscous damping parameter. Using this model, the parameters were determined as $q^* = [6.212 \pm 0.027 \times 10^8 \frac{N}{m^2}, 0.5089 \pm 0.0670 \frac{kg}{m}]$. This is the least accurate damping model with an average percent error of 18.1% between the displacement vectors and the simulated data.

The second model that was examined was the external viscous and internal Kelvin Voigt damping. The estimated parameters then are $q = [E, c_d, \gamma]$ where E is the modulus of elasticity, c_d is the internal strain rate damping coefficient, and γ is the viscous damping parameter. This model performanced much better than viscous damping alone and produced the output $q^* = [6.211 \pm 0.034 \times 10^7 \frac{N}{m^2}, 0.0190 \pm 0.0041 \frac{kg}{m}, 9.232 \pm 0.132 \times 10^4 \frac{kg}{m}]$. The model produced a 8.58 % error between the displacement vectors and the simulated data.

The third model that was examined was the external viscous and internal spatial hysteresis damping. The estimated parameters then are $q = [E, \gamma, a, b]$ where E is the modulus of elasticity, γ is the viscous damping parameter, and a and b are the spatial hysteresis damping coefficients. The parameters using the model were determined to be $q^* = [6.216 \pm 0.038 \times 10^7 \frac{N}{m^2}, 0.0188 \pm 0.0033 \frac{kg}{m}, 6.120 \pm 0.249 \times 10^{-5}, 7.031 \pm 0.065 \times 10^{-4}]$. This model produced a 6.84 % error between the displacement vectors and the simulated data.

6.2 Double Layered Cantilevered Beam

The second beam which was analyzed was a double ply of carbon fiber fabric with a latex membrane. The beam dimensions can be found in Table 6.11.

Table 6.11: Double Beam Parameters

Parameter	Value	Units
Length	0.3048	Meters
Width	0.127	Meters
Height	0.00147	Meters
Mass	0.046	Kilograms

6.2.1 Initial Measurement Plots

The tip displacement was measured over a period of five seconds at 0.003906 second intervals. Five trials were run, each with a slightly different input force. The results from this measurement can be seen in Figure 6.7.

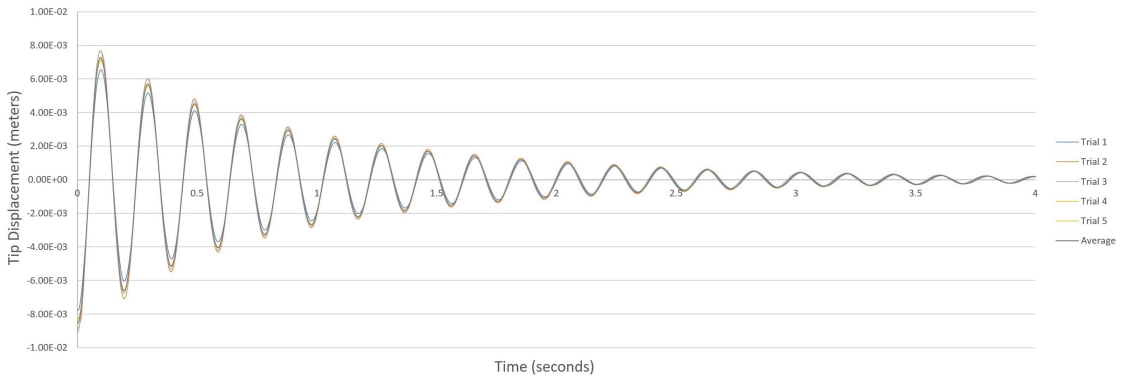

Figure 6.7: Double Ply Cantilever Beam Response

Once again, the period of oscillation remains the same for all five trials. However, as we would expect, the beam dampens much more quickly when double layered than with the single ply beam since the beam is more rigid.

6.2.2 Simulation Results

After this tip data was collected, the inverse parameter estimation was run for each of the trials. These values were then substituted back into the beam equation to compare the simulated data to the experimental data. The results from each of these trials is seen below.

Trial One

Trial 1 was subjected to an initial force $2.148 \times 10^{-3} N$. When the inverse parameter estimation was run for each of the models, it converged at the values seen in Table 6.12.

Table 6.12: Damping Parameter Values for Double Ply Beam Trial 1

	$E\left(\frac{N}{m^2}\right)$	$\gamma\left(\frac{kg}{m}\right)$	$c_d\left(\frac{kg}{m}\right)$	a	b
Viscous	1.382×10^9	3.117	N/A	N/A	N/A
Viscous/KV	8.043×10^7	0.1362	7.021×10^4	N/A	N/A
Viscous/SH	8.042×10^7	0.1210	N/A	5.0176×10^{-5}	1.2129×10^{-4}

These values were put into the beam equation so the simulated data could be compared to the experimental data. The comparison of all three models then is seen in Figure 6.8.

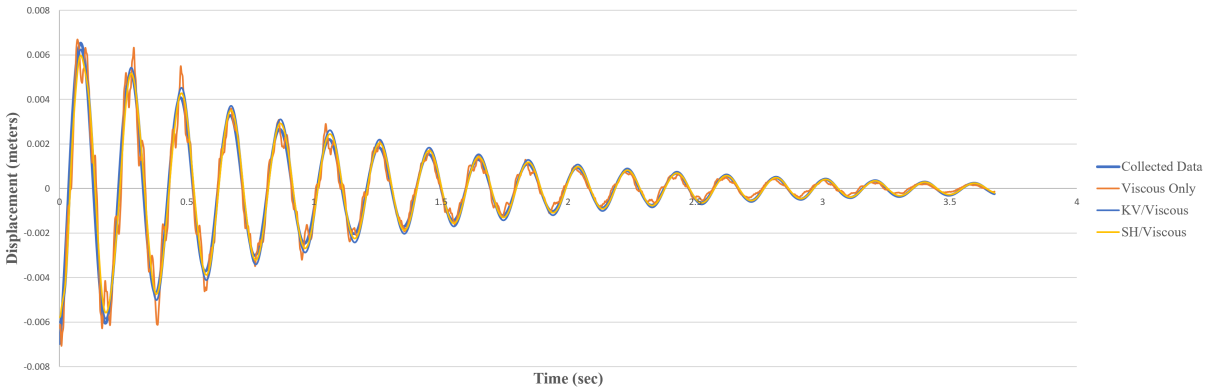

Figure 6.8: Tip Vibration for Double Ply Beam Trial 1

For the three models the error values were:

1. Viscous Damping:
    - Total Error: 0.267736 m
    - Average Error: 0.000284 m
    - Percent Error: 24.47%
2. Viscous and Kelvin Voigt Damping:
    - Total Error: 0.111708 m
    - Average Error: 0.000119 m
    - Percent Error: 10.21%
3. Viscous and Spatial Hysteresis Damping:
    - Total Error: 0.075629 m
    - Average Error: 0.000080 m
    - Percent Error: 6.91%

This process was then repeated for each of the five trials.

Trials Two - Five

Since the same process was repeated four more times, the results have been condensed in the following pages. The initial force for trials 2-5 were

$[2.51 \times 10^{-3}, 3.03 \times 10^{-3}, 2.41 \times 10^{-3}, 2.49 \times 10^{-3}]$ Newtons, respectively. The parameters can be found in Table 6.13, Table 6.14, Table 6.15, and Table 6.16.

Table 6.13: Damping Parameter Values for Double Ply Beam Trial 2

	$E\left(\frac{N}{m^2}\right)$	$\gamma\left(\frac{kg}{m}\right)$	$c_d\left(\frac{kg}{m}\right)$	a	b
Viscous	1.380×10^9	2.716	N/A	N/A	N/A
Viscous/KV	8.066×10^7	0.1364	7.118×10^4	N/A	N/A
Viscous/SH	8.081×10^7	0.1202	N/A	5.819×10^{-5}	1.402×10^{-4}

Table 6.14: Damping Parameter Values for Double Ply Beam Trial 3

	$E\left(\frac{N}{m^2}\right)$	$\gamma\left(\frac{kg}{m}\right)$	$c_d\left(\frac{kg}{m}\right)$	a	b
Viscous	1.389×10^9	2.734	N/A	N/A	N/A
Viscous/KV	8.095×10^7	0.1561	7.220×10^4	N/A	N/A
Viscous/SH	8.101×10^7	0.1215	N/A	5.127×10^{-5}	1.2987×10^{-4}

Table 6.15: Damping Parameter Values for Double Ply Beam Trial 4

	$E\left(\frac{N}{m^2}\right)$	$\gamma\left(\frac{kg}{m}\right)$	$c_d\left(\frac{kg}{m}\right)$	a	b
Viscous	1.381×10^9	2.736	N/A	N/A	N/A
Viscous/KV	8.096×10^7	0.1458	7.182×10^4	N/A	N/A
Viscous/SH	8.099×10^7	0.1218	N/A	4.872×10^{-5}	1.401×10^{-4}

Table 6.16: Damping Parameter Values for Double Ply Beam Trial 5

	$E\left(\frac{N}{m^2}\right)$	$\gamma\left(\frac{kg}{m}\right)$	$c_d\left(\frac{kg}{m}\right)$	a	b
Viscous	1.379×10^9	2.736	N/A	N/A	N/A
Viscous/KV	8.093×10^7	0.1459	7.191×10^4	N/A	N/A
Viscous/SH	8.094×10^7	0.1212	N/A	5.616×10^{-5}	1.410×10^{-4}

These values were put into the beam equation so the simulated data could be compared to the experimental data. Each of the trials have been plotted and can be found in Figure 6.9, Figure 6.10, Figure 6.11, and Figure 6.12.

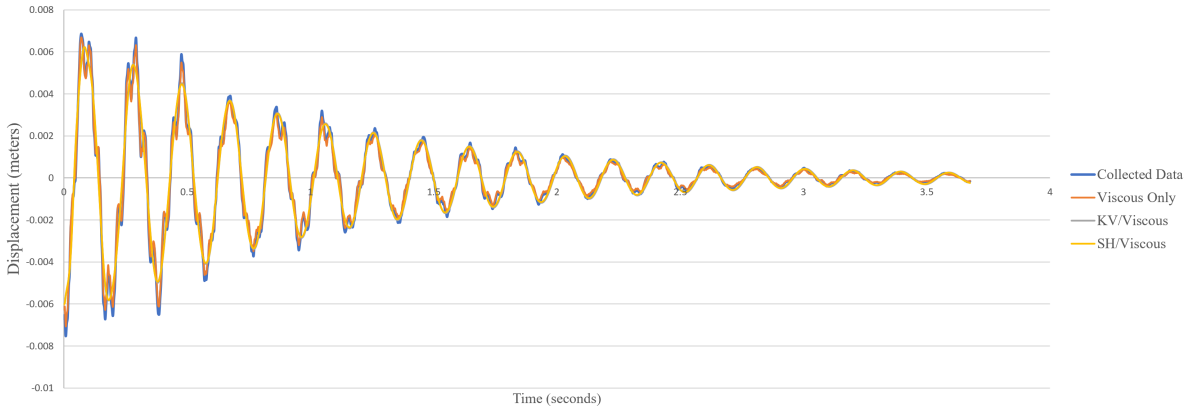

Figure 6.9: Tip Vibration for Double Ply Beam Trial 2

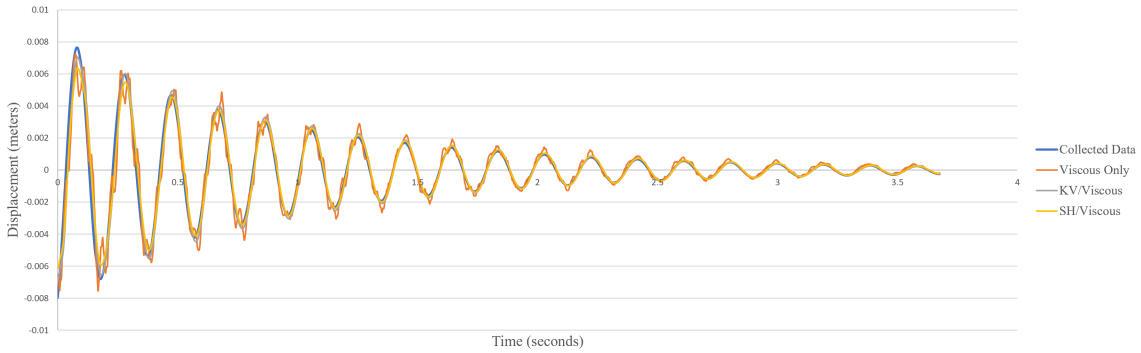

Figure 6.10: Tip Vibration for Double Ply Beam Trial 3

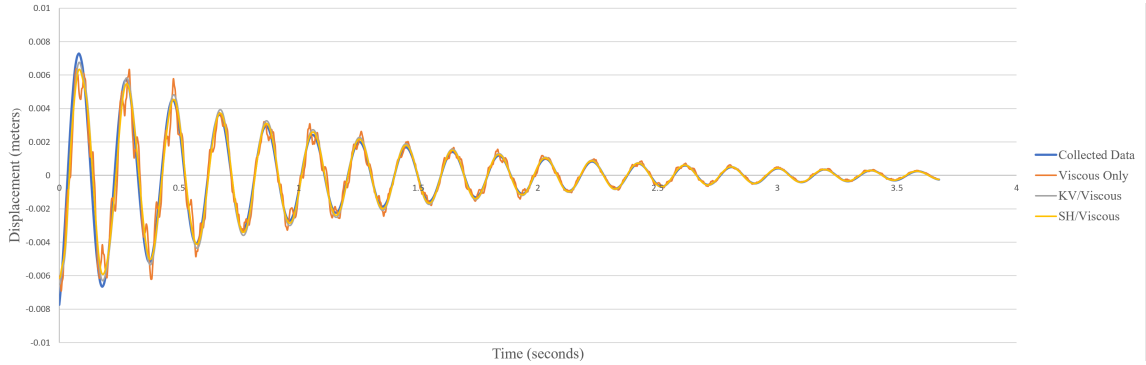

Figure 6.11: Tip Vibration for Double Ply Beam Trial 4

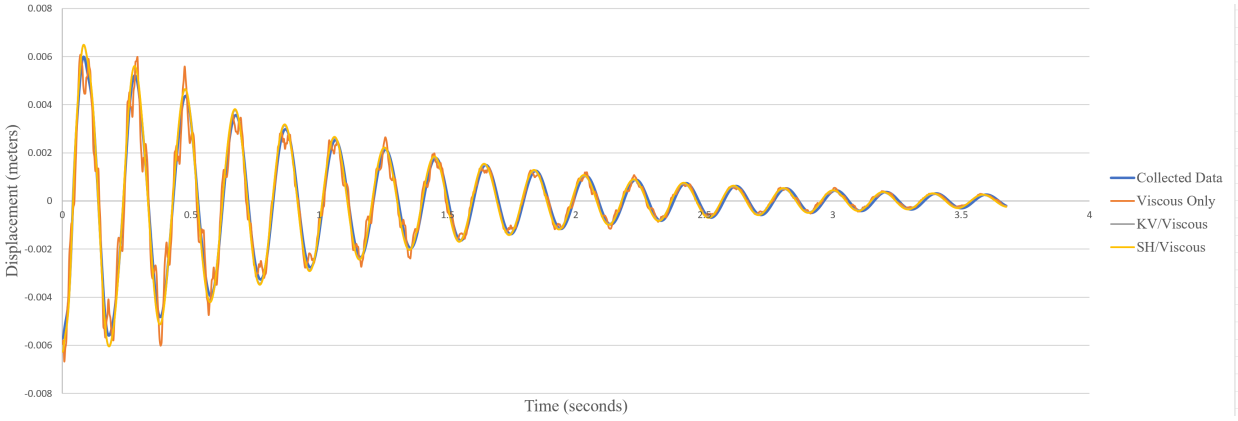

Figure 6.12: Tip Vibration for Double Ply Beam Trial 5

Using the same method as before, the error was calculated for each trial and the results are shown in Table 6.17, Table 6.18, Table 6.19, and Table 6.20.

Table 6.17: Error for Double Ply Beam Trial 2

	Total Error	Average Error	Percent Error
Viscous	0.294304 m	0.000312 m	23.20%
Viscous/KV	0.137470 m	0.000146 m	11.82%
Viscous/SH	0.110142 m	0.000117 m	9.47%

Table 6.18: Error for Double Ply Beam Trial 3

	Total Error	Average Error	Percent Error
Viscous	0.317006 m	0.000337 m	25.98%
Viscous/KV	0.115099 m	0.000122 m	9.43%
Viscous/SH	0.087218 m	0.000093 m	7.15%

Table 6.19: Error for Double Ply Beam Trial 4

	Total Error	Average Error	Percent Error
Viscous	0.277263 m	0.000294 m	23.26%
Viscous/KV	0.118085 m	0.000125 m	9.91%
Viscous/SH	0.064822 m	0.000069 m	5.44%

Table 6.20: Error for Double Ply Beam Trial 5

	Total Error	Average Error	Percent Error
Viscous	0.265866 m	0.000282 m	22.52%
Viscous/KV	0.122188 m	0.000130 m	10.59%
Viscous/SH	0.105627 m	0.000112 m	9.15%

6.2.3 Modal Analysis

Traditional modal analysis is commonly used to estimate the modulus of elasticity. During free vibration, there in no energy input into the system. Since we are modeling the impact as a single impulse, this beam is freely vibrating after impact. We have force and displacement data at the tip of the beam, we can use the beam deflection equation to approximate the modulus of elasticity where delta is the displacement of the beam tip and P is the applied force:

$$\delta = \frac{PL^3}{3EI} \tag{6.12}$$

So, we can rearrange this equation as:

$$E = \frac{PL^3}{3\delta I} \tag{6.13}$$

For each of the five trials, this value is:

$$E_1 = \frac{(2.148 \times 10^{-3}N)(.3048m)^3}{3(0.00750m)\frac{.127m(.00147m^3)}{12}} = 8.04 \times 10^7 \frac{N}{m^2} \tag{6.14}$$

$$E_2 = \frac{(2.508 \times 10^{-3}N)(.3048m)^3}{3(0.00863m)\frac{.127m(.00147m^3)}{12}} = 8.16 \times 10^7 \frac{N}{m^2} \tag{6.15}$$

$$E_3 = \frac{(3.026 \times 10^{-3} N)(.3048m)^3}{3(0.01063m)\frac{.127m(.00147m^3)}{12}} = 7.99 \times 10^7 \frac{N}{m^2} \tag{6.16}$$

$$E_4 = \frac{(2.408 \times 10^{-3} N)(.3048m)^3}{3(0.00852m)\frac{.127m(.00147^3)}{12}} = 7.94 \times 10^7 \frac{N}{m^2} \tag{6.17}$$

$$E_5 = \frac{(2.490 \times 10^{-3} N)(.3048m)^3}{3(0.00865m)\frac{.127m(.00147m^3)}{12}} = 8.08 \times 10^7 \frac{N}{m^2} \tag{6.18}$$

Where the average modulus of elasticity is then calculated as:

$$E = \frac{\sum_{i=1}^{5} E_i}{5} = 8.04 \times 10^7 \frac{N}{m^2} \tag{6.19}$$

And, the standard deviation is:

$$\sigma^2 = \frac{\sum E_i - E}{5} = 0.08 \times 10^7 \frac{N}{m^2} \tag{6.20}$$

This is included to validate that the results obtained throughout the paper are within an appropriate range of the value obtained through an accepted method.

6.2.4 Summary of Results

The first model used only external, viscous damping. The estimated parameters then are $q = [E, \gamma]$ where E is the modulus of elasticity and γ is the viscous damping parameter. Using this model, the parameters were determined as $q^* = [1.338 \pm 0.003 \times 10^9 \frac{N}{m^2}, 2.808 \pm 0.155 \frac{kg}{m}]$. This is the least accurate damping model with an average percent error of 23.89% between the displacement vectors and the simulated data.

The second model that was examined was the external viscous and internal Kelvin Voigt damping. The estimated parameters then are $q = [E, c_d, \gamma]$ where E is the modulus of elasticity, c_d is the internal strain rate damping coefficient, and γ is the viscous damping parameter. This model performanced much better than viscous damping alone and produced

the output $q^* = [8.079 \pm 0.021 \times 10^7 \frac{N}{m^2}, 0.1441 \pm 0.0073 \frac{kg}{m}, 7.146 \pm 0.071 \times 10^4 \frac{kg}{m}]$. The model produced a 10.39 % error between the displacement vectors and the simulated data.

The third model that was examined was the external viscous and internal spatial hysteresis damping. The estimated parameters then are $q = [E, \gamma, a, b]$ where E is the modulus of elasticity, γ is the viscous damping parameter, and a and b are the spatial hysteresis damping coefficients. The parameters using the model were determined to be $q^* = [8.083 \pm 0.022 \times 10^7 \frac{N}{m^2}, 0.1211 \pm 0.0005 \frac{kg}{m}, 5.290 \pm 0.036 \times 10^{-5}, 1.3451 \pm 0.077 \times 10^{-4}]$. This model produced a 7.62 % error between the displacement vectors and the simulated data. Note that, once again, the model converged much quicker when a spatial hysteresis term was included than the other two models.

6.3 Triple Layered Cantilevered Beam

The last beam which was analyzed was a triple ply of carbon fiber fabric with a latex membrane. The beam dimensions are found in Table 6.21.

Table 6.21: Triple Beam Parameters

Parameter	Value	Units
Length	0.3048	Meters
Width	0.127	Meters
Height	0.00198	Meters
Mass	0.071	Kilograms

6.3.1 Initial Measurement Plots

The tip displacement was measured over a period of five seconds at 0.003906 second intervals. Five trials were run, each with a slightly different input force. The results from this measurement can be seen in Figure 6.13.

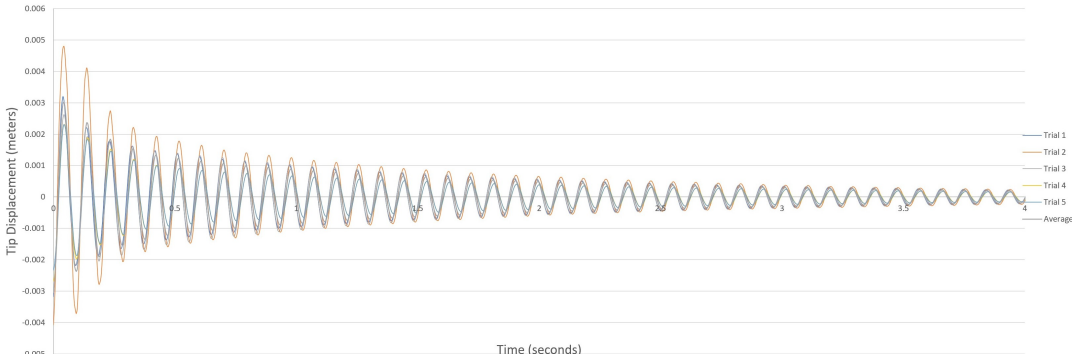

Figure 6.13: Triple Ply Cantilever Beam Data

Since this is a fairly rigid beam, it dampens much quicker than the previous two beams. As we would expect, given we are using an identical beam in each trial, the period remains nearly identical in all five trials. The only difference between the trials are the amplitudes, which are the result of different impact forces.

6.3.2 Simulation Results

After this tip data was collected, the inverse parameter estimation was run for each of the trials. These values were then plugged back into the beam equation to compare the simulated data to the experimental data. The results from each of these trials is seen below.

Trial One

Trial 1 was subjected to an initial force $5.2 \times 10^{-4} N$. When the inverse parameter estimation was run for each of the models, it converged at the values seen in Table 6.22.

Table 6.22: Damping Parameter Values for Triple Ply Beam Trial 1

	$E\left(\frac{N}{m^2}\right)$	$\gamma\left(\frac{kg}{m}\right)$	$c_d\left(\frac{kg}{m}\right)$	a	b
Viscous	2.261×10^9	2.201	N/A	N/A	N/A
Viscous/KV	2.261×10^8	0.241	17.62	N/A	N/A
Viscous/SH	2.261×10^8	0.239	N/A	8.2104×10^{-4}	.001902

These values were put into the beam equation so the simulated data could be compared to the experimental data. The comparison of all three models then is seen below:

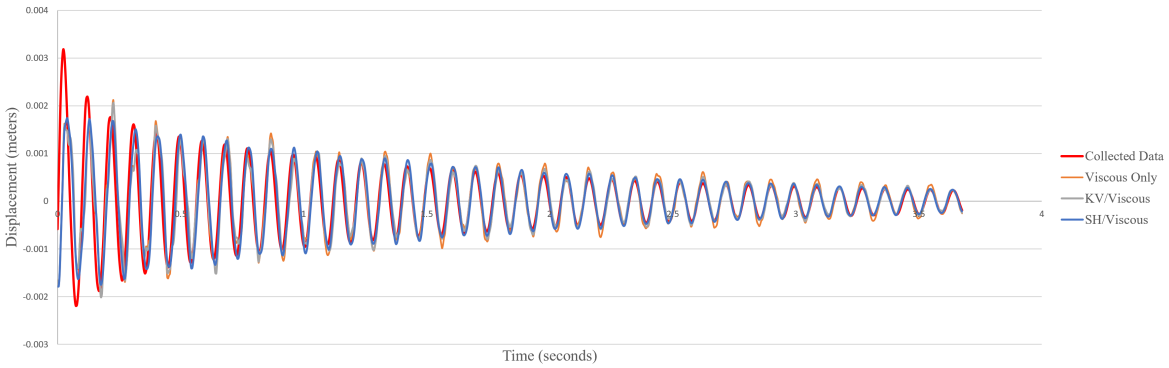

Figure 6.14: Tip Vibration for Triple Ply Beam Trial 1

The total error can be used to find the average error by dividing the total error by the number of trials:

$$\sigma_J = \frac{\sum_{i=1}^{M} |\omega^N(t,l,q) - \hat{\omega}(t,l)|^2}{M}. \tag{6.21}$$

For the three models these values were:

1. Viscous Damping:
    - Total Error: 0.097941 m
    - Average Error: 0.000104 m
    - Percent Error: 21.27%
2. Viscous and Kelvin Voigt Damping:
    - Total Error: 0.081199 m
    - Average Error: 0.000086 m
    - Percent Error: 17.64%
3. Viscous and Spatial Hysteresis Damping:
    - Total Error: 0.068286 m
    - Average Error: 0.000073 m
    - Percent Error: 14.83%

This process was then repeated for each of the five trials.

Trials Two - Five

Since the same process was repeated four more times, the results have been condensed in the following pages. The initial force for trials 2-5 were

$[5.4\times10^{-4}, 1.1\times10^{-4}, 1.20\times10^{-4}, 1.41\times10^{-4}]$ newtons, respectively. The damping parameters are found in Table 6.23, Table 6.24, Table 6.25, and Table 6.26.

Table 6.23: Damping Parameter Values for Triple Ply Beam Trial 2

	$E\left(\frac{N}{m^2}\right)$	$\gamma\left(\frac{kg}{m}\right)$	$c_d\left(\frac{kg}{m}\right)$	a	b
Viscous	2.258×10^9	$2.209\frac{kg}{m}$	N/A	N/A	N/A
Viscous/KV	2.248×10^8	0.245	17.71	N/A	N/A
Viscous/SH	2.259×10^8	0.2392	N/A	8.1117×10^{-4}	.002109

Table 6.24: Damping Parameter Values for Triple Ply Beam Trial 3

	$E\left(\frac{N}{m^2}\right)$	$\gamma\left(\frac{kg}{m}\right)$	$c_d\left(\frac{kg}{m}\right)$	a	b
Viscous	2.261×10^9	2.310	N/A	N/A	N/A
Viscous/KV	2.259×10^8	0.249	17.81	N/A	N/A
Viscous/SH	2.258×10^8	0.2360	N/A	8.2102×10^{-4}	.0022178

Table 6.25: Damping Parameter Values for Triple Ply Beam Trial 4

	$E\left(\frac{N}{m^2}\right)$	$\gamma\left(\frac{kg}{m}\right)$	$c_d\left(\frac{kg}{m}\right)$	a	b
Viscous	2.248×10^9	2.219	N/A	N/A	N/A
Viscous/KV	2.249×10^8	0.250	17.82	N/A	N/A
Viscous/SH	2.252×10^8	0.2390	N/A	9.1002×10^{-4}	.0019802

Table 6.26: Damping Parameter Values for Triple Ply Beam Trial 5

	$E\left(\frac{N}{m^2}\right)$	$\gamma\left(\frac{kg}{m}\right)$	$c_d\left(\frac{kg}{m}\right)$	a	b
Viscous	2.251×10^9	2.224	N/A	N/A	N/A
Viscous/KV	2.249×10^8	0.2530	18.167	N/A	N/A
Viscous/SH	2.251×10^8	0.2370	N/A	8.9002×10^{-4}	.0020416

These values were put into the beam equation so the simulated data could be compared to the experimental data. Each of the trials have been plotted and are shown in Figure 6.15, Figure 6.16, Figure 6.17, and Figure 6.18.

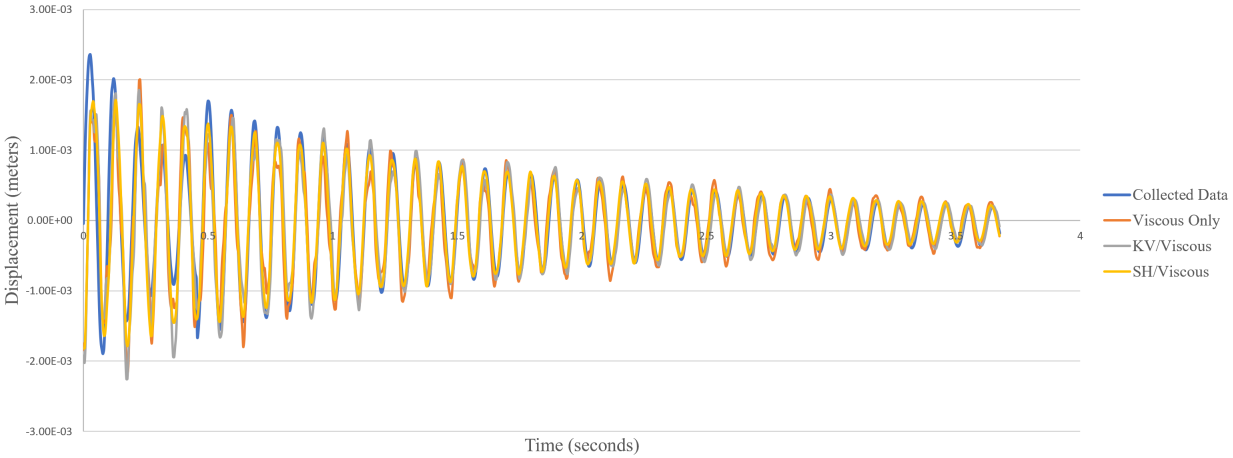

Figure 6.15: Tip Vibration for Triple Ply Beam Trial 2

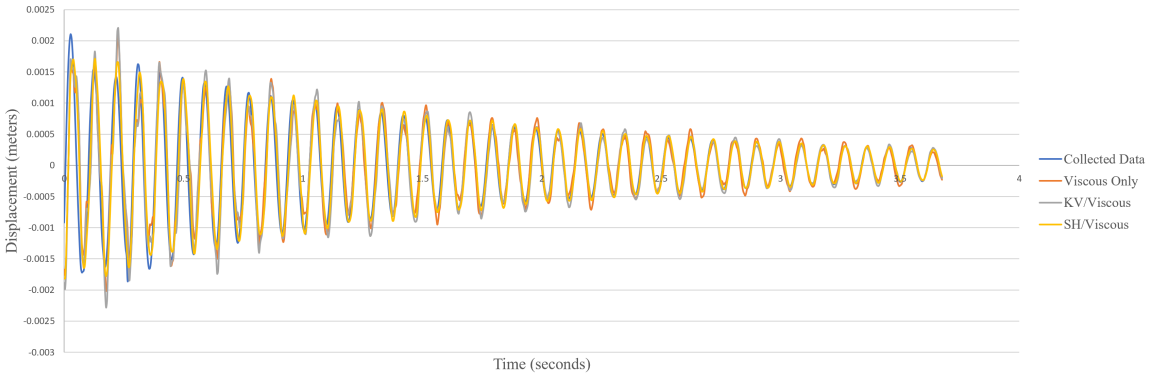

Figure 6.16: Tip Vibration for Triple Ply Beam Trial 3

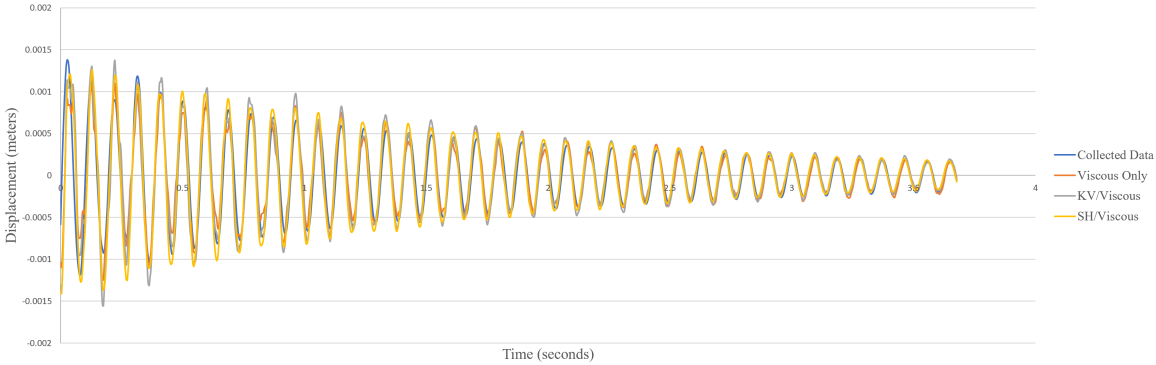

Figure 6.17: Tip Vibration for Triple Ply Beam Trial 4

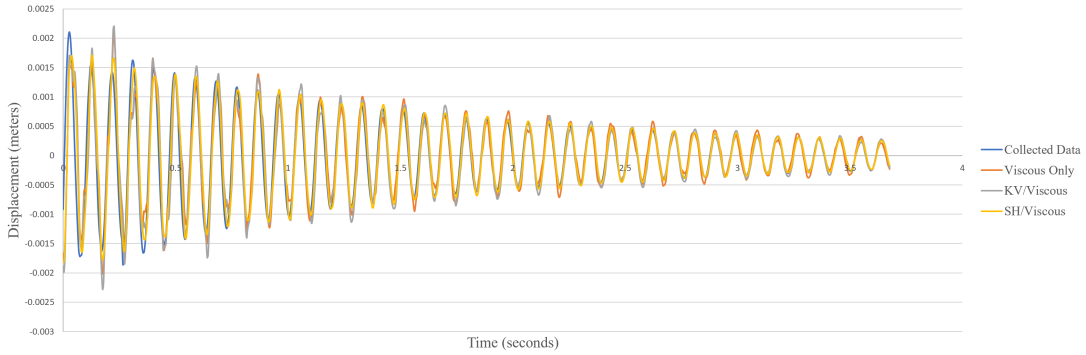

Figure 6.18: Tip Vibration for Triple Ply Beam Trial 5

Using the same method as before, the error was calculated for each trial. These results are seen in Tables 6.27 - 6.30.

Table 6.27: Error for Triple Ply Beam Trial 2

	Total Error	Average Error	Percent Error
Viscous	0.135065 m	0.000143 m	27.93%
Viscous/KV	0.067371 m	0.000072 m	11.44%
Viscous/SH	0.071325 m	0.000076 m	12.11%

Table 6.28: Error for Triple Ply Beam Trial 3

	Total Error	Average Error	Percent Error
Viscous	0.101066 m	0.000107 m	21.67%
Viscous/KV	0.06929 m	0.000074 m	14.31%
Viscous/SH	0.058221 m	0.000062 m	12.02%

Table 6.29: Error for Triple Ply Beam Trial 4

	Total Error	Average Error	Percent Error
Viscous	0.064596 m	0.000069 m	21.25%
Viscous/KV	0.043858 m	0.000047 m	13.01%
Viscous/SH	0.039435 m	0.000419 m	11.69%

Table 6.30: Error for Triple Ply Beam Trial 5

	Total Error	Average Error	Percent Error
Viscous	0.548491 m	0.000582 m	18.87%
Viscous/KV	0.039466 m	0.000042 m	11.94%
Viscous/SH	0.039133 m	0.000042 m	11.84%

6.3.3 Modal Analysis

Traditional modal analysis is commonly used to estimate the modulus of elasticity. During free vibration, there in no energy input into the system. Since we are modeling the impact as a single impulse, this beam is freely vibrating after impact. We have force and displacement data at the tip of the beam, we can use the beam deflection equation to approximate the modulus of elasticity where delta is the displacement of the beam tip and P is the applied force:

$$\delta = \frac{PL^3}{3EI} \tag{6.22}$$

So, we can rearrange this equation as:

$$E = \frac{PL^3}{3\delta I} \tag{6.23}$$

For each of the five trials, this value is:

$$E_1 = \frac{(5.2\times10^{-4}N)(.3048m)^3}{3(0.00472m)\frac{.127m(.00072m^3)}{12}} = 2.63\times10^8\frac{N}{m^2} \tag{6.24}$$

$$E_2 = \frac{(5.4\times10^{-4}N)(.3048m)^3}{3(0.00585m)\frac{.127m(.00072m^3)}{12}} = 2.21\times10^8\frac{N}{m^2} \tag{6.25}$$

$$E_3 = \frac{(1.1\times10^{-4}N)(.3048m)^3}{3(0.00115m)\frac{.127m(.00072m^3)}{12}} = 2.29\times10^8\frac{N}{m^2} \tag{6.26}$$

$$E_4 = \frac{(1.2\times10^{-4}N)(.3048m)^3}{3(0.00098m)\frac{.127m(.00072m^3)}{12}} = 2.93\times10^8\frac{N}{m^2} \tag{6.27}$$

$$E_5 = \frac{(1.4\times10^{-4}N)(.3048m)^3}{3(0.00133m)\frac{.127m(.00072m^3)}{12}} = 2.52\times10^8\frac{N}{m^2} \tag{6.28}$$

Where the average modulus of elasticity is then calculated as:

$$E = \frac{\sum_{i=1}^{5}E_i}{5} = 2.52\times10^8\frac{N}{m^2} \tag{6.29}$$

And, the standard deviation is:

$$\sigma^2 = \frac{\sum E_i - E}{5} = 0.26\times10^8\frac{N}{m^2} \tag{6.30}$$

This is included to validate that the results obtained throughout the paper are within an appropriate range of the value obtained through an accepted method. Traditional modal analysis cannot be used to solve all the beam parameters as it does not work with the hysteresis terms or with spatially dependent parameters. However, it can be used to calculate the modulus of elasticity, which is in relatively good agreement with both the spatial hysteresis and Kelvin Voigt models.

6.3.4 Summary of Results

The first model used only external, viscous damping. The estimated parameters then are $q = [E, \gamma]$ where E is the modulus of elasticity and γ is the viscous damping parameter. Using this model, the parameters were determined as $q^* = [2.256 \pm 0.053\times10^9\frac{N}{m^2}, 2.233 \pm 0.040\frac{kg}{m}]$. This is the least accurate damping model with an average percent error of 23.03% between the displacement vectors and the simulated data.

The second model that was examined was the external viscous and internal Kelvin Voigt damping. The estimated parameters then are $q = [E, c_d, \gamma]$ where E is the modulus of elasticity, c_d is the internal strain rate damping coefficient, and γ is the viscous damping parameter. This model performanced much better than viscous damping alone and produced the output $q^* = [2.253 \pm 0.0533 \times 10^8 \frac{N}{m^2}, 0.2476 \pm 0.0042 \frac{kg}{m}, 17.825 \pm 0.186 \times 10^4 \frac{kg}{m}]$. The model produced a 11.75 % error between the displacement vectors and the simulated data.

The third model that was examined was the external viscous and internal spatial hysteresis damping. The estimated parameters then are $q = [E, \gamma, a, b]$ where E is the modulus of elasticity, γ is the viscous damping parameter, and a and b are the spatial hysteresis damping coefficients. The parameters using the model were determined to be $q^* = [2.256 \pm 0.3967 \times 10^8 \frac{N}{m^2}, 0.2424 \pm 0.0213 \frac{kg}{m}, 8.510 \pm 0.410 \times 10^{-4}, 2.050 \pm 0.011 \times 10^{-3}]$. This model produced a 12.50 % error between the displacement vectors and the simulated data.

6.4 Conclusion on Numerical Results

In summary, we evaluated several flexible, composite cantilever beams. This beam represented a single wing on a MAV. The beams were varying stiffness, as the number of carbon fiber layers varied in each case. The results from these experiments are summarized below.

For a single ply beam, the model using only viscous damping converged on the parameters $q^* = [6.212 \pm 0.027 \times 10^8 \frac{N}{m^2}, 0.5089 \pm 0.0670 \frac{kg}{m}]$ with an average percent error of 18.1% between the displacement vectors and the simulated data. The second model that was examined was the external viscous and internal Kelvin Voigt damping. This

model performanced much better than viscous damping alone and produced the output $q^* = [6.211 \pm 0.034 \times 10^7 \frac{N}{m^2}, 0.0190 \pm 0.0041 \frac{kg}{m}, 9.232 \pm 0.132 \times 10^4 \frac{kg}{m}]$ with a 8.58 % error. The last model was external viscous and internal spatial hysteresis damping. The parameters using the model were determined to be $q^* = [6.216 \pm 0.038 \times 10^7 \frac{N}{m^2}, 0.0188 \pm 0.0033 \frac{kg}{m}, 6.120 \pm 0.249 \times 10^{-5}, 7.031 \pm 0.065 \times 10^{-4}]$ and produced a 6.84 % error between the displacement vectors and the simulated data.

For a double ply beam, these same models converged to the following values; Model 1: $q^* = [1.338 \pm 0.003 \times 10^9 \frac{N}{m^2}, 2.808 \pm 0.155 \frac{kg}{m}]$ with an average percent error of 23.89%, Model 2: $q^* = [8.079 \pm 0.021 \times 10^7 \frac{N}{m^2}, 0.1441 \pm 0.0073 \frac{kg}{m}, 7.146 \pm 0.071 \times 10^4 \frac{kg}{m}]$ with a 10.39 % error, and Model 3: $q^* = [8.083 \pm 0.022 \times 10^7 \frac{N}{m^2}, 0.1211 \pm 0.0005 \frac{kg}{m}, 5.290 \pm 0.036 \times 10^{-5}, 1.3451 \pm 0.077 \times 10^{-4}]$ with a 7.62 % error between the displacement vectors and the simulated data.

For the triple ply beam, the models converged at the following values: Model 1: $q^* = [2.256 \pm 0.053 \times 10^9 \frac{N}{m^2}, 2.233 \pm 0.040 \frac{kg}{m}]$ with an average percent error of 23.03%, Model 2: $q^* = [2.253 \pm 0.0533 \times 10^8 \frac{N}{m^2}, 0.2476 \pm 0.0042 \frac{kg}{m}, 17.825 \pm 0.186 \times 10^4 \frac{kg}{m}]$ with a 11.75 % error, and Model 3: $q^* = [2.256 \pm 0.3967 \times 10^8 \frac{N}{m^2}, 0.2424 \pm 0.0213 \frac{kg}{m}, 8.510 \pm 0.410 \times 10^{-4}, 2.050 \pm 0.011 \times 10^{-3}]$ with a 12.50% error between the displacement vectors and the simulated data.

We made several key observations from the cantilevered beam experiment. We found that, for the two flexible beams, spatial hysteresis damping coupled with viscous air damping produced the most accurate beam model. However, for the rigid beam, the traditional Kelvin Voigt with viscous damping model was actually more accurate of a model. This indicates that, within this framework, spatial hysteresis is more appropriate for very

flexible beams. Also, as the beam got more rigid, all three models produced more error. This is most likely due to inaccuracies in both beam and displacement measurements. Since the beam dampened much quicker, any variation between the calculated and practical values led to a larger error margin.

CHAPTER 7

CONCLUSION

This project aims to identify and address issues of control within a composite, flexible-wing UAV model. By understanding more about the damping model used for such a model, we are more able to understand the dynamics of such an airframe and to incorporate control measures into it. This is paramount for the continued development of micro unmanned aerial vehicle technology.

7.1 Outcome

This project had several significant findings. Most notably, we identified spatial hysteresis damping as a legitimate form of internal damping within small, composite, flexible wing unmanned aerial vehicles. We were able to experimentally validate the inclusion of spatial hysteresis damping into the Euler Bernoulli beam model. This is a key insight into previous experimental and theoretical work. This project also addresses the numerical methods by which a spatially varying beam model is approximated. This is a key component in modeling spatially varying, flexible, composite aircraft wings.

7.2 Future Work

An immediate extension of this work would be to incorporate the spatially varying models into the parameter estimation problem for the damping parameter determination. We

would want to show that, using the spatially varying beam parameters, we could converge on a modulus of elasticity for the length of the beam that varied with position. This would require the collection of beam vibration data over the entire length of the beam. That way, we could examine the way that the parameters spatially vary and build a model upon that data.

Another possible area of research would be to use this research coupled with piezoceramic controller experiments to examine the controllability of such a composite, flexible, morphing-wing model. This would take the model and allow for a controller to be used in the development of UAV technology. This extension would take this project and apply it current technology in the field of UAV development. Likewise, we would be interested in expanding this Euler Bernoulli beam model. Right now, the model only includes heave dynamics. We would be very interested in examining a model with all six degrees of motion.

Bibliography

[1] B. Stanford, "Aeroelastic Analysis and Optimization of Membrane Micro Air Vehicle Wings", University of Florida, 2008.

[2] H.T. Banks and D.J. Inman, "On Damping Mechanisms in Beams", Institute for Computer Applications in Science and Engineering, NASA Langely Research Center, Rep., September 1989.

[3] Walters, J., Evans, K., Chakravarthy, A., and Kuhn, L., "A Comparison of Morphing Control Startegies for a Flexible Wing Micro Air Vehicle Model Incorporating Spatial Hysteresis Damping", IEEE Conference on Decision and Control, Dec 2014.

[4] A. Lin, "Fabrication and Aeroelastic Analysis of Silicone Membrane Micro Air Vehicle Wings", University of Florida, 2009.

[5] Ifju, P., Jenkins, D., Ettinger, S., Lian, Y., Shyy, W., and Waszak, M., "Flexible Wing Based Micro Air Vehicles", AIAA, 2002.

[6] Breuer, K., Swarz, S., Peraire, J., Drela, M., Willis, D., Moss, C., and Batten, B., "Biologically-Inspired Flight for Micro Air Vehicles", Brown University, Providence, RI, July 2012.

[7] Shyy, W., Ifju, P., and Viieru, D., "Membrane Wing-Based Micro Air Vehicles", Applied Mechanics Review, July 2005. Vol. 58, pp. 283-301.

[8] Banks, H., Crowley, J, and Rosen, I., "Methods for the Identification of Material Parameters in Distributed Models for Flexible Structures", Institute for Computer Applications in Science and Engineering, NASA Langely Research Center, Rep., May 1986.

[9] Banks, H., Wang, Y., Inman, D., and Cudney, H., "Parameter Identification Techniques for the Estimation of Damping in Flexible Structure Experiments", IEEE Conference on Decision and Control, Dec. 1987.

[10] Banks, H., Fabiano, R., Wang, Y., Inman, D., and Cudney, H., ”Spatial Versus Time Hysteresis in Damping Mechanisms”, IEEE Conference on Decision and Control, Dec. 1988.

[11] Banks, H. and Rosen, I., ”Computational Methods for the Identification of Spatially Varying Stiffness and Damping in Beams”, Institute for Computer Applications in Science and Engineering, NASA Langely Research Center, Rep., October 1986.

[12] Stewart, J., ”NASA’s Mighty Morphing Wings Make for More Efficient Flying”, Wired Magazine, Nov. 2016.

[13] Stewart, J., ”Highly Flexible Wings”, NASA Television, October 2017.

[14] ”Solid Mechanics,” Section 7.4. Elementary Beam Theory.

[15] Banks, H., Fabiano, R., and Wang, Y., ”Inverse Problem Techniques for Beams with Tip Body and Time Hysteresis Damping”, Institute for Computer Applications in Science and Engineering, NASA Langely Research Center, Rep., April 1989.

[16] Kuhn, L. (August 2011) ”Modeling and Control for Heave Dynamics of a Flexible Wing Micro Aerial Vehicle Distributed Parameter System,” Lousiana Tech University.

[17] Albertani, R., DeLoach, R., Stanford, B., Hubner, J., and Ifju, P. ”Wind Tunnel Testing and Nonlinear Modeling Applied to Powered Micro Air Vehicles with Flexible Wings” AIAA Journal of Aircraft, 45(3), 2008.

[18] Chakravarthy, A., Evans, K., and Evers, J., ”Sensitivities and Functional Gains for a Flexible Aircraft-Inspired Model.” Proceedings of the 2010 American Control Conference, 4893-4898, 2010.

[19] Chakravarthy, A., Evans, K., Evers, J. and Kuhn, L., ”Nonlinear Controllers for Wing Morphing Trajectories of a Heave Dynamics Model.” Proceedings of the 2011 American Control Conference, 2011.

[20] Tian, X., Iriarte-Diaz, J., Middleton, K., Galvao, R., Israeli, E., Roemer, A., Sullivan, A., Song, A., Swartz, S., and Breuer, K., ”Direct Measurements of the Kinematics and Dynamics of Bat Flight.” Bioinspiration and Biomimetics, 2006.

[21] Walker, J., ”Industrial Uses of Drones”, Tech Emergence, July 2017.